

Inhibition of alkaline phosphatase impairs dyslipidemia and protects mice from atherosclerosis

Laurence Bessueille, Lynn Kawtharany, Thibaut Quillard, Claudia Goettsch, Anne Briolay, Nirina Taraconat, Stéphane Balayssac, Véronique Gilard, Saîda Mebarek, Olivier Peyruchaud, et al.

▶ **To cite this version:**

Laurence Bessueille, Lynn Kawtharany, Thibaut Quillard, Claudia Goettsch, Anne Briolay, et al.. Inhibition of alkaline phosphatase impairs dyslipidemia and protects mice from atherosclerosis. Translational Research, The Journal of Laboratory and Clinical Medicine, 2023, 251, pp.2-13. 10.1016/j.trsl.2022.06.010 . hal-03718207

HAL Id: hal-03718207
https://hal.science/hal-03718207

Submitted on 18 Jul 2022

HAL is a multi-disciplinary open access archive for the deposit and dissemination of scientific research documents, whether they are published or not. The documents may come from teaching and research institutions in France or abroad, or from public or private research centers.

L'archive ouverte pluridisciplinaire **HAL**, est destinée au dépôt et à la diffusion de documents scientifiques de niveau recherche, publiés ou non, émanant des établissements d'enseignement et de recherche français ou étrangers, des laboratoires publics ou privés.

Translational Research

Inhibition of alkaline phosphatase impairs dyslipidemia and protects mice from atherosclerosis

--Manuscript Draft--

Manuscript Number:	
Article Type:	Original Research Article
Keywords:	Atherosclerosis, calcification, inflammation, TNAP, liver, metabolic syndrome
Corresponding Author:	David Magne, PhD Lyon 1 University: Universite Claude Bernard Lyon 1 Villeurbanne, FRANCE
First Author:	Laurence Bessueille
Order of Authors:	Laurence Bessueille
	Lynn Kawtharany
	Thibaut Quillard
	Claudia Goettsch
	Anne Briolay
	Nirina Taraconat
	Véronique Gilard
	Saida Mebarek
	Olivier Peyruchaud
	François Duboeuf
	Caroline Bouillot
	Anthony Pinkerton
	Laura Mechtouff
	René Buchet
	Eva Hamade
	Kazem Zibara
	Caroline Fonta
	Emmanuelle Canet-Soulas
	Jose Luis Millan
	David Magne, PhD
Manuscript Region of Origin:	FRANCE
Abstract:	Rationale : calcium accumulation in atherosclerotic plaques predicts cardiovascular mortality, but the mechanisms responsible for plaque calcification and how calcification impacts plaque stability remain debated. Tissue-nonspecific alkaline phosphatase (TNAP) recently emerged as a promising therapeutic target to block cardiovascular calcification. In this study, we sought to investigate the effect of the recently developed TNAP inhibitor SBI-425 on atherosclerosis plaque calcification and progression. Methods: TNAP levels were investigated in ApoE -deficient mice fed a high fat diet from 10 weeks of age and in plaques from the human ECLAGEN biocollection (101 calcified and 14 non-calcified carotid plaques). TNAP was inhibited in mice using SBI-425 administered from 10 to 25 weeks of age, and in human vascular smooth muscle cells (VSMCs) with MLS-0038949. Plaque calcification was imaged in vivo with 18 F-NaF-PET/CT, ex vivo with osteosense, and in vitro with alizarin red. Bone

Powered by Editorial Manager® and ProduXion Manager® from Aries Systems Corporation

	architecture was determined with μCT. Results: TNAP activation preceded and predicted calcification in human and mouse plaques, and TNAP inhibition prevented calcification in human VSMCs and in ApoE -deficient mice. Moreover, TNAP inhibition reduced the blood levels of cholesterol and triglycerides, and protected mice from atherosclerosis, without impacting the skeletal architecture. Metabolomics analysis of liver extracts identified phosphocholine as a substrate of liver TNAP, whose decreased dephosphorylation upon TNAP inhibition likely reduced the release of cholesterol and triglycerides into the blood. Conclusion : systemic inhibition of TNAP protects from atherosclerosis, by ameliorating dyslipidemia, and preventing plaque calcification.
Suggested Reviewers:	Monzur Murshed McGill University monzur.murshed@mcgill.ca expert in vascular calcification; has published important articles on the involvement of alkaline phosphatase in vascular calcification in genetic models.
	Olga Martinez-Augustin omartine@ugr.es Expert in alkaline phosphatase's functions in inflammation and metabolism
	Kristina I Boström kbostrom@mednet.ucla.edu Expert in the molecular and cellular mechanisms leading to vascular calcification

cover letter

Pr David MAGNE
Lyon University
Metabolism, Enzymes and Molecular Mechanisms
ICBMS, CNRS UMR 5246
Bâtiment Raulin ; 43 Bd du 11 novembre 1918
69622 Villeurbanne Cedex, France
Phone: 0033-4-27-46-57-20
Email: david.magne@univ-lyon1.fr

2022-03-16

Dear Professor Jeffrey,

On behalf of all co-authors, I propose for publication in *Translational Research* an article entitled "**Inhibition of alkaline phosphatase impairs dyslipidemia and protects mice from atherosclerosis"**.

We recently published a review article in *Cardiovascular Research* explaining that alkaline phosphatase, the necessary enzyme in bone mineralization, is increasingly suspected to participate in cardiovascular calcification (Goettsch et al, *Cardiovasc Res* 2022). In the present experimental article, we report that alkaline phosphatase is locally associated with calcification in human and mouse atherosclerotic plaques, and that its pharmacological inhibition with the novel inhibitor SBI-425, prevents calcification in human vascular smooth muscle cell cultures *in vitro*, and *in vivo* in aortic plaques of mice with atherosclerosis. More unexpectedly and interestingly, we found that hepatic alkaline phosphatase is activated during the progression of liver steatosis, and that its inhibition reduces the release of triglycerides and cholesterol in the blood, and consequently impairs the whole development of atherosclerotic plaques. We identified phosphocholine as a new substrate of liver alkaline phosphatase, whose dephosphorylation normally participates in the release of lipids from the liver to the blood. Collectively, these data indicate that SBI-425 protects from atherosclerosis through the inhibition of both liver and arterial alkaline phosphatase. They moreover strengthen the notion that alkaline phosphatase inhibition may be a promising therapeutic option for atherosclerosis, especially since we observed that SBI-425 administration reduces inflammation and preserves the bone architecture.

This article is not under consideration for publication elsewhere. All co-authors have read and approved the manuscript.

Yours faithfully,



Brief Commentary

Click here to access/download;Brief Commentary;Brief Commentary.pdf

Click here to view linked References

Brief Commentary

Background:

Our study provides the first demonstration that alkaline phosphatase inhibition prevents atherosclerotic plaque calcification and ameliorates atherosclerosis. Moreover, it identifies an unsuspected function of liver alkaline phosphatase, which is to participate in VLDL release through phosphocholine dephosphorylation.

Translational Significance:

Alkaline phosphatase inhibition has recently emerged as a promising option to block arterial calcification in patients with chronic kidney disease (CKD). Our study suggests that it will also ameliorates atherosclerosis, in patients with, and without CKD. Finally, it provides an unexpected function of liver alkaline phosphatase, whose release in the blood is clinically routinely measured in clinics, but whose function is obscure.

Manuscript Click here to access/download;Manuscript;article text.pdf

Click here to view linked References

Inhibition of alkaline phosphatase impairs dyslipidemia and protects mice from atherosclerosis

Bessueille L[1,*], Kawtharany L[1,*], Quillard T[2], Goettsch C[3], Briolay A[1], Taraconat N[4], Balayssac S[4], Gilard V[4], Mebarek S[1], Peyruchaud O[5], Duboeuf F[5], Bouillot C[6], Pinkerton A[7], Mechtouff L[8,9] Buchet R[1], Hamade E[10], Zibara K[10], Fonta C[11], Canet-Soulas E[9], Millan JL[7], Magne D[1]

[1] Univ Lyon, Université Claude Bernard Lyon 1, UMR CNRS 5246, ICBMS, F69622, LYON, France; [2] Nantes Université, CNRS, INSERM, l'institut du thorax, F-44000 Nantes, France ; [3] Department of Internal Medicine I, Cardiology, Medical Faculty, RWTH Aachen University, Aachen, Germany; [4] Laboratoire des IMRCP, Université de Toulouse, CNRS UMR 5623, Université Toulouse III – Paul Sabatier, France; [5] INSERM, Unit 1033, LYOS, Lyon, France; [6] CERMEP-Imaging Platform, Bron, France. [7] Sanford Burnham Prebys, La Jolla, CA 92037, United States of America; [8] Stroke Department, Hospices Civils de Lyon, France; [9] Univ Lyon, CarMeN Laboratory, INSERM, INRA, INSA Lyon, Université Claude Bernard Lyon 1, Lyon, France; [10] PRASE and Biology Department, Faculty of Sciences - I, Lebanese University, Beirut, Lebanon; [11] Brain and Cognition Research Center CerCo, CNRS UMR5549, Université de Toulouse, France. *both authors contributed equally

Corresponding author: David Magne; Metabolism, Enzymes and Molecular Mechanisms, ICBMS UMR CNRS 5246 University Lyon 1; Batiment Raulin 1er étage, 43 bd du 11 novembre 1918 ; 69622; Villeurbanne cedex, France

Short title: TNAP inhibition ameliorates atherosclerosis

List of abbreviations: Apo: apolipoprotein; bone volume to tissue volume ratio (BV/TV); HFD: high fat diet; LDLR: low density lipoprotein receptor; MetS: metabolic syndrome; NBT/BCIP: nitro blue tetrazolium/5-Bromo-4-chloro-3-indolyl phosphate; NIRF: near-infrared fluorescence; PCR: polymerase chain reaction; PET: positron emission tomography; PP_i: inorganic pyrophosphate; SUVR: standardized uptake value ratio; TNAP: tissue-nonspecific alkaline phosphatase; VSMC: vascular smooth muscle cell.

Abstract

Rationale: calcium accumulation in atherosclerotic plaques predicts cardiovascular mortality, but the mechanisms responsible for plaque calcification and how calcification impacts plaque stability remain debated. Tissue-nonspecific alkaline phosphatase (TNAP) recently emerged as a promising therapeutic target to block cardiovascular calcification. In this study, we sought to investigate the effect of the recently developed TNAP inhibitor SBI-425 on atherosclerosis plaque calcification and progression.

Methods: TNAP levels were investigated in *ApoE*-deficient mice fed a high fat diet from 10 weeks of age and in plaques from the human ECLAGEN biocollection (101 calcified and 14 non-calcified carotid plaques). TNAP was inhibited in mice using SBI-425 administered from 10 to 25 weeks of age, and in human vascular smooth muscle cells (VSMCs) with MLS-0038949. Plaque calcification was imaged *in vivo* with ^{18}F-NaF-PET/CT, *ex vivo* with osteosense, and *in vitro* with alizarin red. Bone architecture was determined with µCT.

Results: TNAP activation preceded and predicted calcification in human and mouse plaques, and TNAP inhibition prevented calcification in human VSMCs and in *ApoE*-deficient mice. Moreover, TNAP inhibition reduced the blood levels of cholesterol and triglycerides, and protected mice from atherosclerosis, without impacting the skeletal architecture. Metabolomics analysis of liver extracts identified phosphocholine as a substrate of liver TNAP, whose decreased dephosphorylation upon TNAP inhibition likely reduced the release of cholesterol and triglycerides into the blood.

Conclusion: systemic inhibition of TNAP protects from atherosclerosis, by ameliorating dyslipidemia, and preventing plaque calcification.

Keywords: Atherosclerosis, calcification, inflammation, TNAP, liver, metabolic syndrome.

Introduction

Cardiovascular diseases are responsible for 17.9 million deaths each year, which represents 31% of all deaths worldwide (https://www.who.int/health-topics/cardiovascular-diseases). Rupture of an atherosclerotic plaque is considered the primary reason for cardiovascular death, accounting for most myocardial infarction cases and about 20% of ischemic strokes [1]. Acknowledged features of vulnerability include a large lipid and necrotic core, a thin fibrous cap and intraplaque hemorrhage [2]. In addition, recent data suggested that microcalcification, characterized by a size less than 10 µm, but not macrocalcification, negatively impact plaque stability [3-5]. Clinically, microcalcification can be discriminated from macrocalcification with ^{18}F-NaF positron emission tomography (PET) [6], because fluoride ions can replace hydroxyl ions in newly formed apatite crystals, but not in more mature, inert macrocalcification. To date, several *ex vivo* and *in vivo* studies have shown that ^{18}F-NaF accumulates in plaques with hallmarks of vulnerability, predicting future events [7-9]. Microcalcification may destabilize plaques through pro-inflammatory and mechanical mechanisms. In human macrophage cultures, crystals measuring from 1 µm to 15 µm induce the release of tumor necrosis factor (TNF)-α at levels inversely associated with crystal size [10, 11]. Microcalcification can also exert a harmful mechanical stress and favor plaque rupture, especially when it develops within the fibrous cap [12-14]. Nonetheless, in the absence of calcification inhibitors that could be used *in vivo*, the real impact of calcification on plaque progression still remains debatable. In this regard, the recent development of an effective specific and *in vivo* inhibitor of tissue-nonspecific alkaline phosphatase (TNAP) should help fill this gap in knowledge [15].

TNAP, the enzyme necessary for physiologic bone and tooth mineralization [16], has emerged as a likely suspect responsible for plaque calcification [reviewed in [17]]. TNAP is normally expressed under the control of the transcription factor RUNX2 in hypertrophic chondrocytes and osteoblasts, where it hydrolyzes the constitutive mineralization inhibitor inorganic pyrophosphate (PP_i), to allow

progression of mineralization onto the extracellular matrix [18, 19]. Interestingly, in atherosclerotic Apolipoprotein (Apo)E-deficient mice, vascular smooth muscle cells (VSMCs) transdifferentiate into chondrocytes and express TNAP before calcification can be detected [20-22]. Moreover, VSMC-specific deletion of RUNX2 in these mice [23], or in atherosclerotic mice deficient for low density lipoprotein receptor (*LDLr*$^{-/-}$) [24], strongly reduces calcification, further suggesting that TNAP is a key player. In humans, where plaque calcification does not seem to involve cartilage formation, and bone formation within only a minority of plaques [25], TNAP from the circulation is suspected to stimulate plaque formation [26, 27]. As its name indicates, TNAP is indeed relatively ubiquitous. In humans, while predominantly expressed in the skeleton and teeth during physiologic mineralization, it is also expressed in the liver and released into the blood in increasing amounts with cholestasis and with the development of metabolic syndrome (MetS) [26, 28-32]. Since genetic deficiency in PP_i generation leads to vascular calcification [33, 34], it is suspected that increased circulating TNAP in MetS exacerbates plaque calcification.

In the present study, we explored the involvement of TNAP in plaque development and calcification in different experimental designs: using ApoE-deficient mice, a biocollection of human carotid plaques as well as cultured human VSMCs. To take into account the ubiquitous nature of TNAP, we also analyzed the effects of its inhibition on the skeleton and liver. We report that systemic TNAP inhibition decreased blood triglyceride and cholesterol levels, and hindered atherosclerosis development, as demonstrated by reduced plaque growth, inflammation and calcification. Importantly, SBI-425 administration exerted these beneficial effects without producing any negative effect on mouse bone architecture.

Materials and methods

Animal experiments

The present project received authorization from the ethics committee of the French Ministry of Education, Research and Innovation (APAFIS#15387-2018060708052279). Two cohorts of mice were used to characterize plaque calcification and TNAP activation (Suppl. Fig. 1A). Six-week-old *ApoE*-deficient male mice (Charles River, Lyon, France) were housed at the animal facility of INSA (Lyon, France; Cetil *n*°C2EA-102), and placed in conventional cages with 5 mice per cage. Mice were maintained on a 12-hrs light-dark cycle (7:00 am-7:00 pm) and were supplied with food and water *ad libitum*. From 10 weeks of age, they were fed *ad libitum* with a high fat diet (HFD, D12108C, Research Diets, New Brunswick, USA) containing 40% fat (kcal) and 1.25% cholesterol (weight). In cohort 1, 8 mice were sacrificed every 2 weeks between weeks 17 to 31, after overnight fasting, for histological and molecular analyses. Total body weight was measured weekly after starting the HFD. The sacrifice was done by CO_2 inhalation after anesthesia with isoflurane and intracardiac blood puncture. The abdominal aorta was used for quantitative polymerase chain reaction (PCR) analyses. We used mice from cohort 2 (n=5 per group) to analyze aortic calcification with ^{18}F-NaF µPET and µCT and to compare the *in vivo* data with the *ex vivo* results obtained in cohort 1. According to the results obtained in cohorts 1 and 2, in the next cohorts (cohorts 3 and 4), we administered the TNAP inhibitor SBI-425 (30 mg/kg/day, formulated as a food admixture in the HFD) from 10 weeks of age [35]. Treatment was stopped at 25 weeks of age, when microcalcification is detected in all mice analyzed in cohorts 1 and 2. Mice in cohort 3 (2 groups of 13 mice) were used for *ex vivo* analysis, and mice in cohort 4 (2 groups of 12 mice) for *in vivo* imaging.

In vivo imaging

Animals were transferred from the animal facility to the Cermep imaging platform (Lyon/Bron, France). Mice were placed into a chamber connected to an isoflurane anesthesia unit. Anesthesia was induced

using an airflow rate of 0.8 L/min and 4% isoflurane, airflow rate was then maintained to 0.6 L/min with 2% isoflurane during the scans. After induction, mice were injected with 0.36 MBq/g of ^{18}F-NaF in 0.1mL saline via tail vein (19 scans) or in retro-orbital venous sinus (16 scans) when the tail veins were not available. After injection, animals were placed in the prone position on the scanning bed. PET-CT images were obtained using a micro PET-CT scanner (Inveon PET-CT, Siemens, Germany). Mice were positioned into the CT system and imaged using the low magnification acquisition settings (acquisition parameters: attenuation mode; projection: 120 ; rotation: 200° ; estimated scan time: 492s ; binning 4x4; effective voxel size: 0.111 x 0.111 x 0.111 mm^3; voltage: 80 kV; current: 500 µA; filter thickness: 0.5 mm; exposure: 200 ms). After CT acquisition, mice were moved into the center of the PET scanner (axial field of view: 127mm). PET acquisition started exactly one hour after ^{18}F-NaF injection, for a total scan time of twenty minutes. Then, mice were allowed to recover into a lead shielded cage. Static images of the 20-min PET acquisitions were reconstructed with attenuation and scatter correction by 3D ordinary Poisson ordered subsets expectation maximization (OP-OSEM3D) with 4 iterations and a zoom factor of 2. The reconstructed volume was constituted of 159 slices of 128 × 128 matrix voxels, with voxel size 0.388 × 0.388 × 0.796 mm^3. CT data were reconstructed using a Feldkamp algorithm with a down sample of 1 (Inveon Acquisition Workplace, Siemens). After reconstruction, the PET and CT data were coregistered. Images were analyzed using Inveon Research workplace (Siemens). The presence of atherosclerotic plaques was evaluated both in CT and PET images. Due to the higher resolution of the CT scan, regions-of-interest (ROI) of the aortic arch were drawn on CT images. Only voxels above the threshold of 390 Hounsfield Unit (calcified structure) were considered. The ROIs were exported onto the coregistered PET images in order to measure ^{18}F-NaF uptake. Standardized uptake value ratio (SUVR) were calculated using the whole body SUV as reference.

Tissue harvest and processing

After euthanasia, the heart and vasculature were perfused with sterile 0.9% NaCl. The aortic root and the aortic arch, with the major arteries that stem from them (brachiocephalic, left common carotid and left subclavian), were dissected under a microscope and frozen in optimal cutting temperature medium (OCT, Thermo Scientific) and stored at -80 °C before serial cryo-sectioning. Abdominal aortas were dissected, rinsed once with sterile phosphate-buffered saline (PBS) pH 7.4, and frozen until RNA extraction. Cryostat sections (5-µm thick) were cut at -21 °C using a Leica CM3050 S cryostat (Leica), mounted on glass slides (SuperFrost Plus Gold glass slides, Thermo scientific) and stored at -80°C until use. Four sections of 5-µm thickness were harvested per slide, yielding 25 to 45 slides per mouse. Prior to analysis, frozen tissue sections were air-dried for 10 min at room temperature and eight consecutive sections were taken from each mouse at 15-µm intervals. Calcification was imaged by near-infrared fluorescence (NIRF) with the calcium tracer osteosense (OS) (PerkinElmer, ex/em 650/680 nm) as previously described [36]. Briefly, frozen sections were treated overnight with OS 680 (1:100) before NIRF imaging. Quantification was performed by computer image analysis using Image J software (NIH, Bethesda, MD) by averaging of measurements from 2 sections of 15 µm apart. Alkaline phosphatase activity was stained in serial sections using nitro blue tetrazolium/5-Bromo-4-chloro-3-indolyl phosphate (NBT/BCIP) solution [37].

To perform CD68 immunohistochemical staining to detect macrophages, serial frozen sections of aortic arch were fixed in acetone (-20 °C) for 10 min and were air-dried afterwards for 10 min. Endogenous peroxidase activity was neutralized with 0.3% H_2O_2 for 10 min followed by 3 washing steps of 5 min each using Tris buffered saline (TBS) pH 7.4 containing 0.025% Triton-X100. Sections were incubated with TBS containing 5% normal goat serum (Abcam) and 1% bovine serum albumin (BSA) for 1 h to reduce non-specific background staining. Sections were subsequently incubated overnight at 4 °C with anti-CD68 antibody (Abcam ab125212) diluted in TBS containing 1% BSA. Horseradish peroxidase-conjugated polyclonal anti-rabbit secondary antibody (Abcam) was applied for 1 h and then revealed with a DAB staining kit (Abcam). Preparations were counterstained with hematoxylin-eosin staining

(Mayer's hematoxylin solution, Sigma). Negative control sections were analyzed using a similar procedure excluding the primary antibody. Images of the sections were captured with an Eclipse TI-E microscope fitted with a DSiQ2 digital camera combined with Nikon's NIS Elements imaging software (Nikon Instruments Inc.). At least 2 sections per mouse were examined for CD68 immunostaining.

For oil Red O staining of neutral lipids, sections were rehydrated in PBS for 5 min, fixed with 10% neutral buffered formalin for 5 min, extensively washed with water, and then treated with propylene glycol for 2 min. The sections were then stained with oil red O solution (0.5% in propylene glycol) for 15 min at 60°C and extensively washed with water. After the oil red O staining procedure, the sections were counterstained with hematoxylin-eosin staining (Mayer's hematoxylin solution, Sigma). Images were captured with an Eclipse TI-E microscope and digital camera (Nikon), combined with Nikon's NIS Elements imaging software. To visualize cartilage glycosaminoglycans, sections were stained with Alcian blue 8GX (Sigma) at pH 2.5 (1% in 3% acetic acid).

Blood biochemistry

Blood was collected from mice by cardiac puncture under anesthesia with isoflurane. After blood coagulation, serum was obtained through centrifugation of the blood for 15 min at 1,500 g at 4°C, frozen in liquid nitrogen and stored at -80°C before analysis. Concentration of total cholesterol and triglycerides were measured using a colorimetric (MAK043, Sigma) and a fluorimetric assay (MAK266, Sigma), respectively. Total bile acids were assayed with a commercial enzyme-based colorimetric kit (Abcam Ab239702). Serum IL-6 and haptoglobin levels were determined using the commercially available ELISA kits (Fischer Scientific 10110623 and Abcam 157714, respectively). The alkaline phosphatase activity assay was adapted from a previously published protocol and performed in a 96-well plate [38]. Briefly, sera were mixed with a concentrated buffer at a ratio of 2.85:1 (vol/vol) in order to get final concentrations of 0.56 M 2-amino-2-methyl-1-propanol buffer pH 10.5, 1 mM $MgCl_2$ and 10 mM *p*-nitrophenylphosphate. Absorbance was acquired for 5 min at 405 nm (Tecan plate reader).

The slope was calculated to determine TNAP activity levels in each sample and normalized to protein amounts measured with the BCA protein assay (Pierce).

Bone parameters

3D microarchitecture of the distal metaphyseal femur and cortical midshaft were carried out using a Skyscan 1176 micro-CT scanner (Skyscan Inc.). The X-ray excitation voltage was set to 50 kV with a current of 500 mA. A 0.5 mm aluminum filter was used to reduce beam-hardening artifacts. Samples were scanned in 70% ethanol with a fixed voxel size of 9.08 µm. Section images were reconstructed with NRecon software (version 1.6.1.8, Skyscan). The region of interest (ROI) to delineate trabecular bone was drawn manually, away from the endocortical surface, starting at 0.5 mm underneath the growth plate and ending at 1.5 mm. For cortical analysis, 0.5 mm on either side of the femur midshaft were reconstructed. The global threshold was set at 0.394 g HA/cm^3. Three-dimensional modeling and analysis of bone volume to tissue volume ratio (BV/TV), trabecular number, trabecular separation, cortical thickness, total porosity, were obtained with the CTAn (version 1.9) and CTVol (version 2.0) software.

Liver biochemistry

For the determination of cholesterol, triglycerides, and total bile acids in the liver, 40-mg pieces of liver were homogenized in 1 mL of 5% NP40 solution in a Dounce homogenizer. The hydrophobic components were extracted twice at 80°C for 5 minutes. Samples were centrifuged and the supernatants were assayed for cholesterol, triglycerides and bile acids with the same kits used for blood. In order to quantify hydroxyproline, 100-mg pieces of liver were homogenized in 1 mL of pure water in a dounce homogenizer and a perchlorate-free kit was used (Sigma, MAK357).

Metabolomics analysis

Liver extraction and NMR measurement: The frozen tissues were weighed and then extracted according to Beckonert's procedure [39] using the methanol-chloroform-water system [2:2:1.425 (v/v/v)], and including absorbance measurement using the Bradford reagent with BSA as standard. The upper methanol/water phase was collected, dried, lyophilized and stored at -80°C. Deuterated phosphate buffer at pH = 7.4 (200 mM) was added to the dried aqueous extract with TSP (sodium 2,2,3,3-tetradeutero-3- trimethylsilylpropionate) (Sigma-Aldrich) as internal chemical shift and quantification reference. ^{1}H NMR spectra were recorded at 298 K on a Bruker Avance spectrometer 500 equipped with a 5-mm TCI cryoprobe. The 1D pulse sequence (relaxation delay-pulse-acquisition) with pre-saturation for water (HOD) signal suppression was used. Acquisition parameters were as follows: relaxation delay 5.64 s, 30° pulse (4.5 µs) and acquisition time of 4.36 s. The spectral width of 15 ppm was used and 256 scans were collected. With this repetition time of 10 s, the ^{1}H resonances were fully relaxed. Data were processed using Bruker TopSpin software 3.2 with one level zero-filling and apodization (exponential, lb = 0.3 Hz) before Fourier transform, then phase correction, simple baseline correction and calibration (δ_{TSP} = 0 ppm) were applied.

Chemometric analysis of NMR data: Data NMR matrices were obtained using facilities included in KnowItAll® (Wiley Science Solutions) and NMRProcFlow® (https://nmrprocflow.org/) [40] software. First, the bucket list was obtained by the bin area method using the intelligent variable size bucketing tool included in the KnowItAll® package according to NMR signals assignment. Second, NMRProcFlow® pipeline was used for local baseline correction of spectra, alignment of NMR signals and integration of NMR area by that bucket list. Then integrated regions were normalized by dividing their areas by that of the internal standard TSP and by the weight of tissue. Statistical analysis, supervised Partial Least Squares-Discriminant Analysis (PLS-DA) and the nonparametric Wilcoxon test were carried out using the SIMCA-P+ 13.0.3 (Sartorius, Aubagne, France) and Matlab® (MathWorks, Natick, Massachusetts, USA) softwares.

^{1}H NMR absolute quantification of metabolites: Metabolites were assigned with an in-house metabolite database at pH = 7.4. A total of 34 metabolites were identified; 30 could be quantified.

Metabolite concentrations (ng/mg liver tissue) were given by $m_x = A_X/A_{TSP}. 9/N_X. 112.M_x/m_L$ with A_X and A_{TSP} being the areas of the signals of metabolite X and TSP, 9 and N_X the number of protons of TSP and metabolite X evoking the signals, 112 the number of nmol of TSP in the solution analyzed, M_x the molecular weight of metabolite X and m the weight (mg) of tissue analyzed.

Human samples

Analysis in human samples has been performed on healthy and diseased carotid arteries. Carotid plaques [n=101 calcified, and 14 non-calcified from the ECLAGEN biocollection [25]] were removed as a single specimen by endarterectomy at the bifurcation from within the lumen. The ECLAGEN biocollection was collected in accordance to the principles outlined in the Declaration of Helsinki. All samples were 1-2 cm long. For histology, we analyzed sections of the lesion core present in each arterial sample. Sample collection and handling were performed in accordance with our institutional medical ethics committee (research protocol#PFS09-014, n°DC-2008-402), and all patients participating in the study provided written informed consent. In the case of organ donors (healthy arteries), the absence of patient opposition to organ donation and an informed and signed consent was required from the patient's family. The arterial samples were fixed in 10% formalin for 48 h, decalcified in 4.13% EDTA-0.2% paraformaldehyde pH 7.4 over 4 days in KOS sw10 (Milestone), and embedded in paraffin. Following heat-induced epitope retrieval in EDTA pH 9, serial sections (4-µm thick) were stained with TNAP (Abcam), and Runx2 (Abcam) antibodies. Imaging of the sections was obtained with the NanoZoomer device (Hamamatsu Photonics).

Human VSMC cultures

Human coronary artery VSMCs (PromoCell) were grown in SMC growth medium 2 (SMC-GM2, PromoCell) supplemented with epidermal growth factor (0.5 ng/mL), insulin (5 µg/mL), basic fibroblast growth factor-β (2 ng/mL), and fetal bovine serum (5%) at 37 °C in humidified 5% CO_2. Cells were used

between passages 3 and 9. Cells from 4-5 independent donors were used. VSMCs were cultured for up to 21 days in the presence of either control medium (DMEM, 10% FBS, 1% penicillin/streptomycin) or osteogenic medium (consisting of control medium supplemented with 10 nM dexamethasone, 10 mM β-glycerophosphate, and 100 µM L-ascorbate phosphate). Media were changed 3 times per week. Mycoplasma contamination test was routinely performed (once a month). TNAP activity was inhibited by the TNAP inhibitor MLS-0038949 (Merck, CAS 496014-13-2), the parent compound of SBI-425 [41]. TNAP activity was determined by the Alkaline Phosphatase Activity Colorimetric Assay Kit (BioVision, San Francisco, USA) according to the manufacturer's instructions. TNAP activity was normalized to the protein amount. To visualize calcification, cells were washed and fixed with 4% paraformaldehyde for 10-15 min at room temperature. The mineralized matrix was visualized by 2% (w/v) Alizarin Red staining (Sigma Aldrich).

Quantitative polymerase chain reaction (PCR) analysis

Mouse tissues: total RNAs were extracted from grinded abdominal aorta or liver with the NucleoSpin RNA II kit (Macherey-Nagel) following the manufacturer's protocol. The quantity and quality of RNA were determined at 260 and 280 nm absorbance with a NanoDrop. RNA (1 µg) was retro-transcribed into cDNA with Superscript II reverse transcriptase (Life Technologies). PCR analysis was conducted using SYBR green Supermix (Biorad) on the iCycler Real-Time Detection system (Biorad). Fold change in mRNA expression was calculated using the $2^{-\Delta Ct}$ method by the CFX Manager software (Biorad). Data were normalized by 3 housekeeping genes (HPRT, Actin and Rpl13a) levels. Primers and PCR conditions are given in Table I. The obtained products were checked by sequencing.

Human VSMCs: total RNA was isolated using TriZol (Life Technologies) and mRNA levels were determined by TaqMan-based real-time PCR (Life Technologies). The following TaqMan probes were used: HS01047978_m1 (human Runx2), HS99999902_m1 (human Rplp0). The expression levels were

normalized to Rplp0. Results were calculated using the ΔΔCt method, and presented as fold increase relative to control.

***In vitro* dephosphorylation of phosphocholine and phosphoethanolamine by TNAP**

25 µM of phosphocholine or phosphoethanolamine were incubated at 37°C with recombinant human TNAP (Biolegend 794504) or mouse TNAP (Biolegend 787804) in a Tris-HCl saline buffer pH 7.4 containing 1 mM $MgCl_2$. After different time points, P_i release was determined using Malachite Green reagent.

Statistics

Data are expressed as the mean ± SEM or SD, as indicated in the Figure legends. Statistical analyses were performed with Past 3.20 software. Data were tested on normality and on equal variances with the Shapiro-Wilk test and Levene test, respectively. Then, data were analyzed on appropriate parametric or nonparametric test, as indicated in the Figure legends. $P<0.05$ was considered significant.

Results

Atherosclerotic plaque calcification is associated with TNAP activity in mouse and human lesions

Our first objective was to determine whether atherosclerotic plaque calcification is associated with TNAP activity in the serum, in the plaques, or in both compartments. To this purpose, we thoroughly characterized where and when calcification initiates in aortas from *ApoE*$^{-/-}$ mice. Aorta calcification was first imaged *in vivo* at 19, 25, 31 and 34 weeks using µCT to quantify calcium volume, and ^{18}F-NaF µPET to determine fluoride incorporation in nascent crystals, and therefore calcification activity (Suppl. Fig. 1A and Fig. 1A). µCT data showed that calcium deposition in the aorta progressed in an almost exponential manner from 19 weeks to 34 weeks of age (Fig. 1B and Suppl. Fig. 1B). Calcification activity also increased from 25 to 31 weeks of age, then it slowed-down between 31 and 34 weeks (Fig. 1C and Suppl. Fig. 1C). Histologically, using the calcium fluorescent dye osteosense, microcalcification of about 10-20 µm in size was detected in the aortic arch, in mice aged 19-21 weeks (Fig. 1D). These first calcified regions grew and fused in the arch until 31 weeks (Fig. 1D,E), to sometimes fill the whole aortic arch (Suppl. Fig. 1D). In parallel, new calcifications appeared in other arteries, such as the left common carotid (Fig. 1D). The total surface of calcifications determined *ex vivo* increased exponentially (Fig. 1F), and similarly to the total volume of calcium measured *in vivo* with µCT (Fig. 1B). We then asked whether TNAP activation in the plaques and/or in the blood was associated with plaque calcification. Strikingly, calcification was consistently associated with TNAP activity in atherosclerotic plaques (Fig. 1G). Moreover, TNAP activity was commonly detected in aortic plaques from 17-19 week-old mice (Fig. 1H), suggesting that TNAP activation preceded microcalcification, and was responsible for its formation. On the other hand, serum TNAP activity remained unchanged from 17 to 31 weeks (Suppl. Fig. 1E). These results strongly suggested that local TNAP, but not liver or circulating TNAP, participated in plaque calcification in *ApoE*$^{-/-}$ mice.

We next wondered which cells expressing TNAP might be involved in atherosclerotic plaque calcification. In *ApoE*$^{-/-}$ mice, calcification was shown to develop into cartilaginous metaplasia [20]. However, there is still some uncertainty as to whether plaque calcification in these mice is induced by hypertrophic chondrocytes, or whether like in humans, in association with calcifying macrophages [42], or with macrophage debris [43]. Like in Rattazzi's characterization of *ApoE*$^{-/-}$ mice [20], macrocalcification unambiguously developed within cartilaginous metaplasia, as firstly demonstrated by the colocalization of osteosense and alcian blue staining (Fig 2A). Moreover, the expression pattern of the chondrocyte differentiation markers *Sox9*, *Acan*, *Runx2* and *Alpl* (Fig. 2B) was very similar to the calcification activity measured with ^{18}F-NaF µPET, with a rise from 25 weeks followed by a plateau (Fig. 1C). In these cartilaginous metaplasia, macrocalcification likely relied on TNAP expressed by hypertrophic chondrocytes. Indeed, the evolution of *Alpl* transcripts encoding TNAP was very similar to that of the chondrocyte marker *Acan*, and strongly associated with that of the transcription factor *Runx2*, known to stimulate chondrocyte hypertrophy and *Alpl* expression (Fig. 2B,C). Finally, these cartilaginous macrocalcifications were devoid of CD68-positive cells (Fig. 2A), suggesting that macrophages did not directly participate in their growth. On the other hand, microcalcification was often observed in locations enriched in macrophages, and not yet positive for alcian blue staining for cartilage glycosaminoglycans (Fig. 2A). Therefore, it is possible that, before growing within cartilaginous metaplasia, microcalcification formed in association with TNAP in macrophage-like cells [42]. In conclusion, these first data collectively suggested that TNAP, expressed in plaques by hypertrophic chondrocytes and/or macrophages, was responsible for plaque calcification in *ApoE*$^{-/-}$ mice.

We then sought to investigate whether TNAP is also locally associated with calcifications in human carotid plaques. This was more uncertain because cartilage metaplasia has never been reported in human plaques, and because bone metaplasia occurs less frequently, and predominantly in peripheral arteries [25]. We analyzed a biocollection of human carotid plaques in which the calcification morphology

has been characterized in details [25]. In these lesions and independently of the calcification size and morphology, TNAP was consistently located at the proximal periphery of calcifications (Fig. 3). Interestingly, TNAP was expressed in both RUNX2-positive and RUNX2-negative cells. Considered together, these results in humans and mice strongly suggested that TNAP is involved in plaque calcification. To validate this hypothesis in *ApoE*$^{-/-}$ mice, we chose to inhibit TNAP in a preventive manner, from 10 weeks of age, by administrating 30 mg/kg/day of SBI-425 admixed in the HFD [35]. This treatment was stopped at 25 weeks to determine the involvement of TNAP in the initiation of plaque calcification.

TNAP inhibition in mice decreases cholesterolemia and reduces atherosclerotic plaque development

As recently shown in other disease models [15, 44], SBI-425 administration was well-tolerated, with no effect on food intake, weight gain, or all-cause mortality (Suppl. Fig. 2A). Moreover, not only TNAP inhibition did not deteriorate trabecular or cortical bone architecture, but also it tended to preserve it, although not at a statistically significant level (Suppl. Fig. 2B). Even more unexpectedly, while TNAP inhibition had no significant effect on serum glucose and non-esterified fatty acids (NEFAs), it strongly decreased the levels of triglycerides (TGs) and cholesterol (Fig. 4). Since hypercholesterolemia is the driving force for atherosclerosis in *ApoE*$^{-/-}$ mice [45], SBI-425 treatment also affected atherogenesis. If the plaques of mice treated with SBI-425 presented similar levels of lipid content (%) (Fig. 5A,B), they were significantly smaller (Figure 5A,C). Moreover, TNAP inhibition also decreased aortic inflammation, as demonstrated by the significant reduction in the relative levels of the inflammatory markers *Cd68*, *Rankl*, *Opn*, *Il8*, *Il1b*, *Il6* (Fig. 5D), and tended to reduce serum IL-6 concentration (Fig. 5E). Calcium accumulation and calcification activity were also impaired, as determined *in vivo* with µCT and ^{18}F-NaF µPET (Fig. 5F and 5G respectively). Histological analyses with osteosense, which in our hands was the most sensitive method for this imaging, detected calcification in only 4 mice out of 12 treated with SBI-425 (33%), whereas all control mice presented with calcification (Fig. 5H). The reduction of plaque calcification in mice treated with SBI-425 probably resulted from the beneficial

effect of SBI-425 on cholesterolemia and plaque development. Indeed, TNAP inhibition not only prevented calcification, but it also prevented cartilage formation, as illustrated by the absence of alcian blue-positive cartilaginous metaplasia in aortic plaques that were devoid of calcification (Fig. 5B). Nevertheless, SBI-425 also likely prevented calcification by directly inhibiting TNAP activity in plaques. We already reported that TNAP inhibition prevents calcification in cultured mouse VSMCs trans-differentiated into chondrocytes [46]. We report here that TNAP was activated in human VSMCs stimulated to trans-differentiate into osteochondrocyte-like cells, and that its inhibition also prevented calcification (Suppl. Fig. 3). Collectively, these data suggested that SBI-425 administration impaired atherosclerosis by reducing blood cholesterol levels, and locally inhibited plaque calcification. Since in *ApoE*$^{-/-}$ mice, blood cholesterol is predominantly transported by liver-derived very low density lipoproteins (VLDLs) [45], we next explored the effects of SBI-425 on the liver.

Liver TNAP reduces hypercholesterolemia by dephosphorylating phosphocholine

Transcript levels of *Alpl,* encoding TNAP, showed a broad peak between 19 and 27 weeks in the liver of *ApoE*$^{-/-}$ mice (Fig. 6A), which was concomitant with the accumulation of cholesterol (Fig. 6B) and TGs (Fig. 6C) in the liver, and the release of TGs in the blood (Fig. 6D). Moreover, there was a positive correlation between *Alpl* transcript levels and the TG content in the liver in 25-week-old mice (Fig. 6D). Inhibition of TNAP from 10 to 25 weeks did not change the liver content of cholesterol (Fig. 6F) and TGs (Fig. 6G). Since TNAP inhibition reduced the levels of TGs and cholesterol in the circulation but not in the liver, these results suggested that liver TNAP participated in their release. We therefore hypothesized that TNAP inhibition induced liver inflammation or fibrosis to exert these effects through VLDL release. However, SBI-425 administration had no effect on liver inflammation, as revealed by the levels of *Ly6g*, *Tnfa*, *Il1b* or *Hb* transcripts (Fig. 6H), and by the concentration of the liver acute phase protein haptoglobin in the blood (Fig. 6I). Moreover, it did not impact liver fibrosis, as demonstrated by the similar contents of hydroxyproline in treated and untreated mice (Fig. 6J).

Then, to further identify the mechanisms explaining how TNAP inhibition decreased serum lipid levels while unaffecting lipid content in the liver, we used a metabolomics approach to determine hepatic metabolites whose levels were significantly impacted by SBI-425 administration. Multivariate statistical analysis on metabolomics data (PLS-DA) for the 30 detected metabolites, did not show any major impact of TNAP inhibition on liver metabolism (Suppl. Fig. 2C). Nevertheless, TNAP inhibition seemed to decrease phosphocholine levels in the liver (Fig. 6K, p=0.07), a phosphorylated compound and thus a putative TNAP substrate. Extracellular phosphocholine dephosphorylation in the liver is necessary to allow choline uptake in hepatocytes [47], intracellular synthesis of phosphocholine, and generation of phosphatidylcholine, which is required for VLDL production and TG and cholesterol release in the blood [48]. This mechanism explains why choline-deficient diets or genetic deficiency in liver phosphatidylcholine production result in liver steatosis, reduced VLDL levels and impaired atherosclerosis in *ApoE*-deficient mice [49, 50]. This possible decrease in liver phosphocholine was moreover intriguing considering the recent report that TNAP-deficient mice develop exacerbated liver steatosis when fed a HFD but not a choline-deficient diet [51]. We therefore believe that TNAP-dependent inhibition of phosphocholine dephosphorylation in the liver by SBI-425 administration, likely contributed to the beneficial effects of SBI-425 on serum lipids and atherosclerosis. Indeed, we observed a significant inverse relationship between the content of phosphocholine and the levels of cholesterol and TGs in the liver, indicating that when phosphocholine content was the most reduced by SBI-425 administration, the liver content of TGs and cholesterol was the highest (Fig. 6L). Moreover, we provide here evidence that phosphocholine is a TNAP substrate. The quantification of P_i release from phosphocholine in presence or absence of the parental inhibitor of SBI-425 (MLS-0038949), indicated that mouse and human recombinant TNAP were equally potent in dephosphorylating phosphocholine (Fig. 6M). Finally, the cholesterol that was not released in VLDLs in mice treated with SBI-425 was probably transformed into bile acids (BAs) since the liver content of BA was almost significantly increased by SBI-425 treatment (Fig. 6N). Unfortunately, we did not harvest the bile and

could not explore whether bile excretion was increased by TNAP inhibition in *ApoE*$^{-/-}$ mice, as it is in rats [52].

Discussion

The main finding of this study is that the systemic pharmacological inhibition of TNAP prevented dyslipidemia and protected *ApoE*$^{-/-}$ mice from atherosclerosis and plaque calcification. These beneficial effects most likely relied on the inhibition of liver TNAP. Like in humans, whom liver TNAP production and release in the blood are associated with the development of MetS [26-32], hepatic TNAP expression in *ApoE*$^{-/-}$ mice showed a similar trend as TG levels in liver and serum. We provide here evidence that a function of this hepatic TNAP is to participate in the release of lipids from hepatocytes into circulating VLDLs. Indeed, when TNAP was inhibited, the levels of lipids in the blood were significantly reduced. TNAP may be the yet unknown phosphatase that dephosphorylates phosphocholine in the liver, to allow the uptake of choline in hepatocytes [47]. In the mouse liver, TNAP is mainly expressed in endothelial cells [53], where probably reside ENPP6, the enzyme that generates phosphocholine from glycerophosphocholine, and where is suspected to be the phosphatase hydrolyzing phosphocholine into choline [47]. Following its uptake in hepatocytes, intracellular choline is then rephosphorylated into phosphocholine to generate phosphatidylcholine, which is the main phospholipid involved in VLDL production [48]. This hypothesis is appealing because choline deficiency or genetic deficiency in liver phosphatidylcholine production reduces blood cholesterol levels and impairs atherosclerosis in *ApoE*-deficient mice [48-50]. Phosphocholine levels in the liver showed a strong tendency to decrease in response to SBI-425 administration *in vivo*. In addition, mouse and human TNAP were equally potent in dephosphorylating phosphocholine *in vitro*. However, why TNAP inhibition did not exacerbate liver steatosis in *ApoE*$^{-/-}$ mice remains elusive, since choline-deficient diets induce liver steatosis [49]. We suspect that steatosis was prevented because of the previously described liver TNAP function in bile excretion. In addition to being active in liver endothelial cells, hepatic TNAP is also localized in the membrane of hepatocytes and cholangiocytes facing bile canaliculi and ducts [53-56]. At this location, TNAP is thought to reduce the secretory processes of the intrahepatic biliary epithelium, as demonstrated by the significant increase in bicarbonate secretion and basal bile flow induced by TNAP

inhibition in rats [52]. Since in our experiments, TNAP inhibition tended to increase the content of bile acids in the liver, we suspect that cholesterol catabolism into bile acids and bile acid excretion were also enhanced, thereby preventing steatosis.

To summarize, TNAP inhibition limited atherosclerosis development, likely through impaired phosphocholine dephosphorylation, decreased choline uptake and phosphatidylcholine production in hepatocytes, and reduced TG and cholesterol release in VLDLs. This reduction in atherosclerotic development was reflected in mice treated with SBI-425 by smaller plaques in aortas, with less inflammation, and less calcification. While the decrease in plaque size and inflammation likely resulted from the inhibition of liver TNAP, the strong reduction in the number of aortic calcifications in mice treated with SBI-425 probably also relied on the inhibition of local TNAP blockade. Indeed, we observed that in mouse and human plaques, TNAP expression preceded calcification, and colocalized with calcium deposits once they had formed. Moreover, TNAP inhibition in human VSMCs stimulated to calcify totally prevented calcium deposition. This result is consistent with previous report by Tani et al, showing that SBI-425 treatment efficiently blocked vascular calcification in a mouse model of chronic kidney disease (CKD) [44].

In conclusion, TNAP inhibition might represent a promising therapeutic option, not only to prevent vascular calcification in patients with CKD, but also to reduce hypercholesterolemia and atherosclerosis development in individuals with MetS, in whom TNAP levels are associated with mortality risk [26-32]. In our experiments in *ApoE*$^{-/-}$ mice, SBI-425 administration for 15 weeks did not induce negative effects in plaques, blood, liver or bones. While TNAP activation during liver disease in mice fed a HFD was proposed to participate in the dephosphorylation and detoxification of lipopolysaccharide (LPS) [57], we observed no increase in serum LPS levels in animals treated with SBI-425 as compared to controls (data not shown). Moreover, administration of SBI-425 tended to decrease, and not increase, circulating IL-6 levels, and those of the acute phase protein haptoglobin,

indicating that systemic and liver inflammation were probably reduced, and not increased by SBI-425. Finally, SBI-425 administration not only did not lead to bone architecture degradation, but instead also tended to increase the bone volume as compared to untreated animals. Mice treated with SBI-425 seemed globally healthier than untreated mice; they were less dyslipidemic and less inflammatory, explaining why their bones were preserved despite the important function of TNAP in bone mineralization.

Funding

This study was funded by European Research Area Network on Cardiovascular Diseases (ERA-CVD, Microexploration project 2018-2021) and by the “Fondation de France” (project 00086497). Part of the metabolomic studies were supported by the Association Hypophosphatasie Europe (contract 194679).

Conflict of interest

JLM and AP are co-inventors on a patent covering SBI-425 (PCT WO 2013126608). Other authors declare no competing financial or non-financial interests.

References

1. Ornello R, Degan D, Tiseo C, Di Carmine C, Perciballi L, Pistoia F, Carolei A, Sacco S. Distribution and Temporal Trends From 1993 to 2015 of Ischemic Stroke Subtypes: A Systematic Review and Meta-Analysis. *Stroke* 2018;**49**:814-819.
2. Silvestre-Roig C, de Winther MP, Weber C, Daemen MJ, Lutgens E, Soehnlein O. Atherosclerotic plaque destabilization: mechanisms, models, and therapeutic strategies. *Circ Res* 2014;**114**:214-226.
3. Karlöf E, Seime T, Dias N, Lengquist M, Witasp A, Almqvist H, Kronqvist M, Gådin JR, Odeberg J, Maegdefessel L, Stenvinkel P, Matic LP, Hedin U. Correlation of computed tomography with carotid plaque transcriptomes associates calcification with lesion-stabilization. *Atherosclerosis* 2019;**288**:175-185.
4. Shioi A, Ikari Y. Plaque Calcification During Atherosclerosis Progression and Regression. *J Atheroscler Thromb* 2018;**25**:294-303.
5. Bos D, Arshi B, van den Bouwhuijsen QJA, Ikram MK, Selwaness M, Vernooij MW, Kavousi M, van der Lugt A. Atherosclerotic Carotid Plaque Composition and Incident Stroke and Coronary Events. *J Am Coll Cardiol* 2021;**77**:1426-1435.
6. Irkle A, Vesey AT, Lewis DY, Skepper JN, Bird JL, Dweck MR, Joshi FR, Gallagher FA, Warburton EA, Bennett MR, Brindle KM, Newby DE, Rudd JH, Davenport AP. Identifying active vascular microcalcification by (18)F-sodium fluoride positron emission tomography. *Nat Commun* 2015;**6**:7495.
7. Joshi NV, Vesey AT, Williams MC, Shah AS, Calvert PA, Craighead FH, Yeoh SE, Wallace W, Salter D, Fletcher AM, van Beek EJ, Flapan AD, Uren NG, Behan MW, Cruden NL, Mills NL, Fox KA, Rudd JH, Dweck MR, Newby DE. (18)F-fluoride positron emission tomography for identification of ruptured and high-risk coronary atherosclerotic plaques: a prospective clinical trial. *Lancet* 2013.
8. Vesey AT, Jenkins WS, Irkle A, Moss A, Sng G, Forsythe RO, Clark T, Roberts G, Fletcher A, Lucatelli C, Rudd JH, Davenport AP, Mills NL, Al-Shahi Salman R, Dennis M, Whiteley WN, van Beek EJ, Dweck MR, Newby DE. F-Fluoride and. *Circ Cardiovasc Imaging* 2017;**10**.
9. Mechtouff L, Sigovan M, Douek P, Costes N, Le Bars D, Mansuy A, Haesebaert J, Bani-Sadr A, Tordo J, Feugier P, Millon A, Luong S, Si-Mohamed S, Collet-Benzaquen D, Canet-Soulas E, Bochaton T, Crola Da Silva C, Paccalet A, Magne D, Berthezene Y, Nighoghossian N. Simultaneous assessment of microcalcifications and morphological criteria of vulnerability in carotid artery plaque using hybrid. *J Nucl Cardiol* 2020.
10. Nadra I, Mason JC, Philippidis P, Florey O, Smythe CD, McCarthy GM, Landis RC, Haskard DO. Proinflammatory activation of macrophages by basic calcium phosphate crystals via protein kinase C and MAP kinase pathways: a vicious cycle of inflammation and arterial calcification? *Circ Res* 2005;**96**:1248-1256.
11. Nadra I, Boccaccini AR, Philippidis P, Whelan LC, McCarthy GM, Haskard DO, Landis RC. Effect of particle size on hydroxyapatite crystal-induced tumor necrosis factor alpha secretion by macrophages. *Atherosclerosis* 2008;**196**:98-105.
12. Kelly-Arnold A, Maldonado N, Laudier D, Aikawa E, Cardoso L, Weinbaum S. Revised microcalcification hypothesis for fibrous cap rupture in human coronary arteries. *Proc Natl Acad Sci U S A* 2013;**110**:10741-10746.
13. Maldonado N, Kelly-Arnold A, Vengrenyuk Y, Laudier D, Fallon JT, Virmani R, Cardoso L, Weinbaum S. A mechanistic analysis of the role of microcalcifications in atherosclerotic plaque stability: potential implications for plaque rupture. *Am J Physiol Heart Circ Physiol* 2012;**303**:H619-628.
14. Vengrenyuk Y, Carlier S, Xanthos S, Cardoso L, Ganatos P, Virmani R, Einav S, Gilchrist L, Weinbaum S. A hypothesis for vulnerable plaque rupture due to stress-induced debonding

around cellular microcalcifications in thin fibrous caps. *Proc Natl Acad Sci U S A* 2006;**103**:14678-14683.
15. Sheen CR, Kuss P, Narisawa S, Yadav MC, Nigro J, Wang W, Chhea TN, Sergienko EA, Kapoor K, Jackson MR, Hoylaerts MF, Pinkerton AB, O'Neill WC, Millán JL. Pathophysiological role of vascular smooth muscle alkaline phosphatase in medial artery calcification. *J Bone Miner Res* 2014.
16. Millán JL, Whyte MP. Alkaline Phosphatase and Hypophosphatasia. *Calcif Tissue Int* 2016;**98**:398-416.
17. Goettsch C, Strzelecka-Kiliszek A, Bessueille L, Quillard T, Mechtouff L, Pikula S, Canet-Soulas E, Millán JL, Fonta C, Magne D. TNAP as a therapeutic target for cardiovascular calcification - a discussion of its pleiotropic functions in the body. *Cardiovasc Res* 2020.
18. Harmey D, Hessle L, Narisawa S, Johnson KA, Terkeltaub R, Millán JL. Concerted regulation of inorganic pyrophosphate and osteopontin by akp2, enpp1, and ank: an integrated model of the pathogenesis of mineralization disorders. *Am J Pathol* 2004;**164**:1199-1209.
19. Hessle L, Johnson KA, Anderson HC, Narisawa S, Sali A, Goding JW, Terkeltaub R, Millan JL. Tissue-nonspecific alkaline phosphatase and plasma cell membrane glycoprotein-1 are central antagonistic regulators of bone mineralization. *Proc Natl Acad Sci U S A* 2002;**99**:9445-9449.
20. Rattazzi M, Bennett BJ, Bea F, Kirk EA, Ricks JL, Speer M, Schwartz SM, Giachelli CM, Rosenfeld ME. Calcification of advanced atherosclerotic lesions in the innominate arteries of ApoE-deficient mice: potential role of chondrocyte-like cells. *Arterioscler Thromb Vasc Biol* 2005;**25**:1420-1425.
21. Rosenfeld ME, Polinsky P, Virmani R, Kauser K, Rubanyi G, Schwartz SM. Advanced atherosclerotic lesions in the innominate artery of the ApoE knockout mouse. *Arterioscler Thromb Vasc Biol* 2000;**20**:2587-2592.
22. Aikawa E, Nahrendorf M, Figueiredo JL, Swirski FK, Shtatland T, Kohler RH, Jaffer FA, Aikawa M, Weissleder R. Osteogenesis associates with inflammation in early-stage atherosclerosis evaluated by molecular imaging in vivo. *Circulation* 2007;**116**:2841-2850.
23. Sun Y, Byon CH, Yuan K, Chen J, Mao X, Heath JM, Javed A, Zhang K, Anderson PG, Chen Y. Smooth muscle cell-specific runx2 deficiency inhibits vascular calcification. *Circ Res* 2012;**111**:543-552.
24. Lin ME, Chen TM, Wallingford MC, Nguyen NB, Yamada S, Sawangmake C, Zhang J, Speer MY, Giachelli CM. Runx2 deletion in smooth muscle cells inhibits vascular osteochondrogenesis and calcification but not atherosclerotic lesion formation. *Cardiovasc Res* 2016;**112**:606-616.
25. Espitia O, Chatelais M, Steenman M, Charrier C, Maurel B, Georges S, Houlgatte R, Verrecchia F, Ory B, Lamoureux F, Heymann D, Gouëffic Y, Quillard T. Implication of molecular vascular smooth muscle cell heterogeneity among arterial beds in arterial calcification. *PLoS One* 2018;**13**:e0191976.
26. Tonelli M, Curhan G, Pfeffer M, Sacks F, Thadhani R, Melamed ML, Wiebe N, Muntner P. Relation between alkaline phosphatase, serum phosphate, and all-cause or cardiovascular mortality. *Circulation* 2009;**120**:1784-1792.
27. Panh L, Ruidavets JB, Rousseau H, Petermann A, Bongard V, Bérard E, Taraszkiewicz D, Lairez O, Galinier M, Carrié D, Ferrières J. Association between serum alkaline phosphatase and coronary artery calcification in a sample of primary cardiovascular prevention patients. *Atherosclerosis* 2017;**260**:81-86.
28. Lammers WJ, van Buuren HR, Hirschfield GM, Janssen HL, Invernizzi P, Mason AL, Ponsioen CY, Floreani A, Corpechot C, Mayo MJ, Battezzati PM, Parés A, Nevens F, Burroughs AK, Kowdley KV, Trivedi PJ, Kumagi T, Cheung A, Lleo A, Imam MH, Boonstra K, Cazzagon N, Franceschet I, Poupon R, Caballeria L, Pieri G, Kanwar PS, Lindor KD, Hansen BE, Group GPS. Levels of alkaline phosphatase and bilirubin are surrogate end points of outcomes of patients with primary biliary cirrhosis: an international follow-up study. *Gastroenterology* 2014;**147**:1338-1349.e1335; quiz e1315.

29. Abramowitz M, Muntner P, Coco M, Southern W, Lotwin I, Hostetter TH, Melamed ML. Serum alkaline phosphatase and phosphate and risk of mortality and hospitalization. *Clin J Am Soc Nephrol* 2010;**5**:1064-1071.
30. Krishnamurthy VR, Baird BC, Wei G, Greene T, Raphael K, Beddhu S. Associations of serum alkaline phosphatase with metabolic syndrome and mortality. *Am J Med* 2011;**124**:566.e561-567.
31. Wannamethee SG, Sattar N, Papcosta O, Lennon L, Whincup PH. Alkaline phosphatase, serum phosphate, and incident cardiovascular disease and total mortality in older men. *Arterioscler Thromb Vasc Biol* 2013;**33**:1070-1076.
32. Filipowicz R, Greene T, Wei G, Cheung AK, Raphael KL, Baird BC, Beddhu S. Associations of serum skeletal alkaline phosphatase with elevated C-reactive protein and mortality. *Clin J Am Soc Nephrol* 2013;**8**:26-32.
33. Rutsch F, Ruf N, Vaingankar S, Toliat MR, Suk A, Höhne W, Schauer G, Lehmann M, Roscioli T, Schnabel D, Epplen JT, Knisely A, Superti-Furga A, McGill J, Filippone M, Sinaiko AR, Vallance H, Hinrichs B, Smith W, Ferre M, Terkeltaub R, Nürnberg P. Mutations in ENPP1 are associated with 'idiopathic' infantile arterial calcification. *Nat Genet* 2003;**34**:379-381.
34. Nitschke Y, Baujat G, Botschen U, Wittkampf T, du Moulin M, Stella J, Le Merrer M, Guest G, Lambot K, Tazarourte-Pinturier MF, Chassaing N, Roche O, Feenstra I, Loechner K, Deshpande C, Garber SJ, Chikarmane R, Steinmann B, Shahinyan T, Martorell L, Davies J, Smith WE, Kahler SG, McCulloch M, Wraige E, Loidi L, Höhne W, Martin L, Hadj-Rabia S, Terkeltaub R, Rutsch F. Generalized arterial calcification of infancy and pseudoxanthoma elasticum can be caused by mutations in either ENPP1 or ABCC6. *Am J Hum Genet* 2012;**90**:25-39.
35. Romanelli F, Corbo A, Salehi M, Yadav MC, Salman S, Petrosian D, Rashidbaigi OJ, Chait J, Kuruvilla J, Plummer M, Radichev I, Margulies KB, Gerdes AM, Pinkerton AB, Millán JL, Savinov AY, Savinova OV. Overexpression of tissue-nonspecific alkaline phosphatase (TNAP) in endothelial cells accelerates coronary artery disease in a mouse model of familial hypercholesterolemia. *PLoS One* 2017;**12**:e0186426.
36. Goettsch C, Hutcheson JD, Aikawa M, Iwata H, Pham T, Nykjaer A, Kjolby M, Rogers M, Michel T, Shibasaki M, Hagita S, Kramann R, Rader DJ, Libby P, Singh SA, Aikawa E. Sortilin mediates vascular calcification via its recruitment into extracellular vesicles. *J Clin Invest* 2016;**126**:1323-1336.
37. Lencel P, Delplace S, Pilet P, Leterme D, Miellot F, Sourice S, Caudrillier A, Hardouin P, Guicheux J, Magne D. Cell-specific effects of TNF-α and IL-1β on alkaline phosphatase: implication for syndesmophyte formation and vascular calcification. *Lab Invest* 2011;**91**:1434-1442.
38. Sergienko EA, Sun Q, Ma CT. A method for direct assessment of tissue-nonspecific alkaline phosphatase (TNAP) inhibitors in blood samples. *Methods Mol Biol* 2013;**1053**:103-113.
39. Beckonert O, Keun HC, Ebbels TM, Bundy J, Holmes E, Lindon JC, Nicholson JK. Metabolic profiling, metabolomic and metabonomic procedures for NMR spectroscopy of urine, plasma, serum and tissue extracts. *Nat Protoc* 2007;**2**:2692-2703.
40. Jacob D, Deborde C, Lefebvre M, Maucourt M, Moing A. NMRProcFlow: a graphical and interactive tool dedicated to 1D spectra processing for NMR-based metabolomics. *Metabolomics* 2017;**13**:36.
41. Pinkerton AB, Sergienko E, Bravo Y, Dahl R, Ma CT, Sun Q, Jackson MR, Cosford NDP, Millán JL. Discovery of 5-((5-chloro-2-methoxyphenyl)sulfonamido)nicotinamide (SBI-425), a potent and orally bioavailable tissue-nonspecific alkaline phosphatase (TNAP) inhibitor. *Bioorg Med Chem Lett* 2018;**28**:31-34.
42. Kawakami R, Katsuki S, Travers R, Romero DC, Becker-Greene D, Passos LSA, Higashi H, Blaser MC, Sukhova GK, Buttigieg J, Kopriva D, Schmidt AM, Anderson DG, Singh SA, Cardoso L, Weinbaum S, Libby P, Aikawa M, Croce K, Aikawa E. S100A9-RAGE Axis Accelerates Formation of Macrophage-Mediated Extracellular Vesicle Microcalcification in Diabetes Mellitus. *Arterioscler Thromb Vasc Biol* 2020;**40**:1838-1853.

43. Jinnouchi H, Sato Y, Sakamoto A, Cornelissen A, Mori M, Kawakami R, Gadhoke NV, Kolodgie FD, Virmani R, Finn AV. Calcium deposition within coronary atherosclerotic lesion: Implications for plaque stability. *Atherosclerosis* 2020.
44. Tani T, Fujiwara M, Orimo H, Shimizu A, Narisawa S, Pinkerton AB, Millán JL, Tsuruoka S. Inhibition of tissue-nonspecific alkaline phosphatase protects against medial arterial calcification and improves survival probability in the CKD-MBD mouse model. *J Pathol* 2020;**250**:30-41.
45. Meir KS, Leitersdorf E. Atherosclerosis in the apolipoprotein-E-deficient mouse: a decade of progress. *Arterioscler Thromb Vasc Biol* 2004;**24**:1006-1014.
46. Bessueille L, Fakhry M, Hamade E, Badran B, Magne D. Glucose stimulates chondrocyte differentiation of vascular smooth muscle cells and calcification: A possible role for IL-1β. *FEBS Lett* 2015.
47. Morita J, Kano K, Kato K, Takita H, Sakagami H, Yamamoto Y, Mihara E, Ueda H, Sato T, Tokuyama H, Arai H, Asou H, Takagi J, Ishitani R, Nishimasu H, Nureki O, Aoki J. Structure and biological function of ENPP6, a choline-specific glycerophosphodiester-phosphodiesterase. *Sci Rep* 2016;**6**:20995.
48. Li Z, Vance DE. Phosphatidylcholine and choline homeostasis. *J Lipid Res* 2008;**49**:1187-1194.
49. Corbin KD, Zeisel SH. Choline metabolism provides novel insights into nonalcoholic fatty liver disease and its progression. *Curr Opin Gastroenterol* 2012;**28**:159-165.
50. Cole LK, Dolinsky VW, Dyck JR, Vance DE. Impaired phosphatidylcholine biosynthesis reduces atherosclerosis and prevents lipotoxic cardiac dysfunction in ApoE-/- Mice. *Circ Res* 2011;**108**:686-694.
51. Gámez-Belmonte R, Tena-Garitaonaindia M, Hernández-Chirlaque C, Córdova S, Ceacero-Heras D, de Medina FS, Martínez-Augustin O. Deficiency in Tissue Non-Specific Alkaline Phosphatase Leads to Steatohepatitis in Mice Fed a High Fat Diet Similar to That Produced by a Methionine and Choline Deficient Diet. *Int J Mol Sci* 2020;**22**.
52. Alvaro D, Benedetti A, Marucci L, Delle Monache M, Monterubbianesi R, Di Cosimo E, Perego L, Macarri G, Glaser S, Le Sage G, Alpini G. The function of alkaline phosphatase in the liver: regulation of intrahepatic biliary epithelium secretory activities in the rat. *Hepatology* 2000;**32**:174-184.
53. Halling Linder C, Englund UH, Narisawa S, Millán JL, Magnusson P. Isozyme profile and tissue-origin of alkaline phosphatases in mouse serum. *Bone* 2013.
54. Hoshi K, Amizuka N, Oda K, Ikehara Y, Ozawa H. Immunolocalization of tissue non-specific alkaline phosphatase in mice. *Histochem Cell Biol* 1997;**107**:183-191.
55. Araki N, Takashima Y, Makita T. Redistribution and fate of colchicine-induced alkaline phosphatase in rat hepatocytes: possible formation of autophagosomes whose membrane is derived from excess plasma membrane. *Histochem Cell Biol* 1995;**104**:257-265.
56. Chida K, Taguchi M. Localization of alkaline phosphatase and proteins related to intercellular junctions in primary cultures of fetal rat hepatocytes. *Anat Embryol (Berl)* 2005;**210**:75-80.
57. Schippers M, Post E, Eichhorn I, Langeland J, Beljaars L, Malo MS, Hodin RA, Millán JL, Popov Y, Schuppan D, Poelstra K. Phosphate Groups in the Lipid A Moiety Determine the Effects of LPS on Hepatic Stellate Cells: A Role for LPS-Dephosphorylating Activity in Liver Fibrosis. *Cells* 2020;**9**.

Figure legends

Figure 1: TNAP activity is locally associated with plaque calcification in mice. Representative *in vivo* imaging of aortic calcification (red arrow) with µCT (top) and ^{18}F-NaF µPET/µCT (bottom) in a 34-week-old mouse (A), and its quantification by µCT (B) and ^{18}F-NaF µPET (C). Histological analysis of calcification after osteosense (OS) staining in *ApoE*-deficient mice at 21 weeks, 25 weeks and 31 weeks (D). Quantification of calcification number (E) and surface (F) after OS staining at 17 (n=8), 19 (n=8), 21 (n=8), 23 (n=8), 25 (n=6), 27 (n=6), 29 (n=6) and 31 weeks (n=8). TNAP activity staining in the aortic arch shown in D at 21 weeks (G). OS staining and TNAP activity staining in a 19-week-old mouse (H). All quantitative results are shown as mean ± standard deviation, and statistical analyses were performed with one way ANOVA (F) and student's t-test (B, C, E, H). CT: computed tomography; NC: necrotic core; OS: osteosense; PET: positron emission tomography; SUVR: standardized uptake value ratio.

Figure 2: Calcification-associated TNAP is mainly produced by hypertrophic chondrocytes in mouse plaques. Histological analysis of calcification (with OS, top), of glycosaminoglycans (with alcian blue, center), and of CD68 expression (by IHC, bottom), in a 31-week-old *ApoE*-deficient mice (A). Relative transcripts levels in the aorta from 17 to 31 weeks (B). Correlation between *Alpl* and *Runx2* levels from 17 to 31 weeks, as calculated with Pearson's test (C). Quantitative results in C are shown as mean ± standard deviation, and statistical analyses were performed with student's t-test. AA: aortic arch; BC: brachiocephalic artery; IHC: Immunohistochemistry; LCC: left common carotid; LSC: left subclavian.

Figure 3: TNAP, expressed in RUNX2-positive and –negative cells, is locally associated with calcifications in human atherosclerotic plaques. Representative IHC staining of TNAP and RUNX2 in a human calcified carotid atherosclerotic plaque. Calcifications are indicated by *. On the central, low-

magnification (x 2.5) photographs, the bar indicates 1 mm; on the high-magnification images (x 40), the bar indicates 50 µm. IHC: immunohistochemistry.

Figure 4: TNAP inhibition decreases the blood levels of triglycerides and cholesterol. Quantification in the serum of *ApoE*-deficient mice of the levels of glucose, NEFAs, TGs and cholesterol. Results are shown as mean ± standard deviation, and statistical analyses were performed with student's t-test (TGs and cholesterol) or Mann-Whitney (glucose and NEFAs). NEFA: non-esterified fatty acid; TG: triglyceride.

Figure 5: TNAP inhibition reduces atherosclerotic plaque development. Histological analysis of lipids (with Oil red O, top), calcification (with OS, center), and glycosaminoglycans (with alcian blue, bottom) in 25-week-old *ApoE*-deficient mice untreated (left) or treated with SBI-425 (right) (A). Quantification of Oil red O surface (B) and plaque surface (C). Relative transcripts levels in the aorta (D); IL-6 levels in the serum (E). Quantification of aorta calcification by µCT (F) and calcification activity with ^{18}F-NaF µPET (G). Quantification of calcification number (H) and surface (I) after OS staining. Results are shown as mean ± standard deviation, and statistical analyses were performed with student's t-test (C-E) or Mann-Whitney (F-I). CT: computed tomography; OS: osteosense; PET: positron emission tomography; SUVR: standardized uptake value ratio.

Figure 6: TNAP participates in choline metabolism and lipid release from the liver.

Evolution in ApoE-deficient mice from 17 to 31 weeks, of the relative *Alpl* transcripts (A), cholesterol content (B), TG content (C). Quantification of serum TGs in ApoE-deficient mice from 17 to 31 weeks (D). Association between the relative *Alpl* transcripts and the content of TGs in the liver (E). Effect of SBI-425 administration from 10 weeks to 25 weeks, on liver cholesterol content (F), liver TG content (G), relative transcripts levels of inflammatory markers (H), serum haptogloblin levels (I), and liver

content of hydroxyproline (J) and phosphocholine (K). Association between liver phosphocholine levels and liver levels of TGs or cholesterol (L). Dephosphorylation of phosphocholine by mouse or human TNAP in presence (MLS) or absence (CT) of MLS-0038949 (M). Levels of bile acids in the liver (N). Results are shown as mean ± standard deviation, and statistical analyses were performed with student's t-test. Correlations were calculated with Pearson's test. BA: bile acids; TG: triglycerides.

Supplemental Figure 1: *ApoE*-deficient mice fed a HFD from 10 weeks of age, were analyzed every two weeks after sacrifice (cohort 1), and *in vivo* at 19, 25, 31 and 34 weeks (cohort 2) (A). *in vivo* quantification of calcification with µCT (B) and ^{18}F-NaF µPET (C) (each color represents a mouse). OS staining of a calcification filling the whole aortic arch (left) within a cartilaginous metaplasia (right, stained with alcian blue) in a 25-week-old mouse (D). TNAP activity in the serum from 17 to 31 weeks (E). CT: computed tomography; HFD: high fat diet; PET: positron emission tomography; SUVR: standardized uptake value ratio.

Supplemental Figure 2: Weight gain in *ApoE*-deficient mice treated (SBI) or not (CT) with SBI-425 in cohort 3; † indicates a death (A). Bone architecture parameters determined at 25 weeks in *ApoE*-deficient mice treated or not with SBI-425 in cohort 3 (B, n=7 per group). Quantification of metabolite levels in the liver (C, ng/mg of tissue) as determined by NMR-metabolomics. Results are shown as mean ± standard deviation. BMD: bone mineral density; BV: bone volume; GMP: guanidine monophosphate; NAD: nicotinamide adenine dinucleotide; NADP: nicotinamide adenine dinucleotide phosphate; NMR: nuclear magnetic resonance; TV: total volume.

Supplemental Figure 3: Alizarin red staining of calcium deposits in representative cultures of human VSMCs grown in CM or OM for 7, 14 or 21 days (A). Evolution during time of TNAP activity in human VSMCs cultured in CM or OM (B). Effect of MLS-0038949 inhibitor of TNAP on calcification (C), TNAP activity (D), and *RUNX2* transcript levels (E) at 21 weeks. Results are shown as mean ± standard

deviation, and statistical analyses were performed with Mann-Whitney U test. CM: control medium; MLS: MLS-0038949; OM: osteogenic medium; VSMC: vascular smooth muscle cell.

Table(s) Click here to access/download;Table(s);Table 1.pdf

Table I: summary of primers used. Shown are the mouse (m) and human (h) primer sequences (F: forward; R: reverse), annealing temperatures (Ta), base pair (bp) lengths of the corresponding PCR products, and GenBank accession numbers.

Gene (bp)	GenBank	Ta (°C)	Sequence	Length
m*Acan*	NM_007424.2	60	F: 5′ - GTGCGGTACCAGTGCACTGA-3′ R: 5′ - GGGTCTGTGCAGGTGATTCG-3′	104
m*Actin*	NM_007393.3	60	F: 5′ - AATTTCTGAATGGCCCAGGT-3′ R: 5′ - GGTAAGGTGTGCACTTTTATTGG-3′	156
m*Alpl*	NM_007431.3	60	F: 5′ - CAAAGGCTTCTTCTTGCTGGT-3′ R: 5′ - AAGGGCTTCTTGTCCGTGTC-3′	258
m*Cd68*	NM_001291058.1	60	F: 5′ - ATCCCCACCTGTCTCTCTCA -3′ R: 5′ - TTGCATTTCCACAGCAGAAG -3′	216
m*Hp*	NM_017370.2	60	F: 5′- TGAGGCAGTGTGTGGGAAG-3′ R: 5′- TGGCGGGAGATCATCTTG-3′	114
m*Hprt*	NM_013556.2	60	F: 5′ - AGGACCTCTCGAAGTGT-3′ R: 5′ - ATTCAAATCCCTGAAGTACTCAT-3′	111
m*Il-1ß*	NM_008361.4	60	F: 5′ -GGGCCTCAAAGGAAAGAATC-3′ R: 5′ -CCACTTTGCTCTTGACTTCTATC-3′	152
m*Il-6*	NM_031168	60	F: 5′ -GTCACAGAAGGAGTGGCTA-3′ R: 5′ -AGAGAACAACATAAGTCAGATACC-3′	193
m*Il-8*	NM_008176.3	47	F: 5′ - AAACTAATATTTATTGGG-3′ R: 5′ - TTTCAAGACATACAAACA-3′	155
m*Ly6g*	NM_001310438.1	60	F: 5′- TTGCAAAGTCCTGTGTGCT-3′ R: 5′- AGGGGCAGGTAGTTGTGTTG-3′	126
m*Opn*	NM_001204203.1	60	F: 5′ - CTTTCACTCCAATCGTCCCTA-3′ R: 5′ - GCTCTCTTTGGAATGCTCAAGT-3′	305
m*Runx2*	NM_009820.5	60	F: 5′ - GCCGGGAATGATGAGAACTA-3′ R: 5′ - GGACCGTCCACTGTCACTTT-3′	200
m*Rpl13a*	NM_009438.5	60	F: 5′ - ATCCCTCCACCCTATGACAA-3′	97

			R: 5′ - GCCCCAGGTAAGCAAACTT-3′	
m*Sox9*	NM_011448.4	60	F: 5′ - GTACCCGCATCTGCACAAC-3′ R: 5′ - CTCCTCCACGAAGGGTCTCT-3′	94
m*Tnfa*	NM-013693	60	F: 5′ -TGGGACAGTGACCTGGACTGT-3′ R: 5′ -TTCGGAAAGCCCATTTGAGT-3′	67

Figure(s)

Figure 1

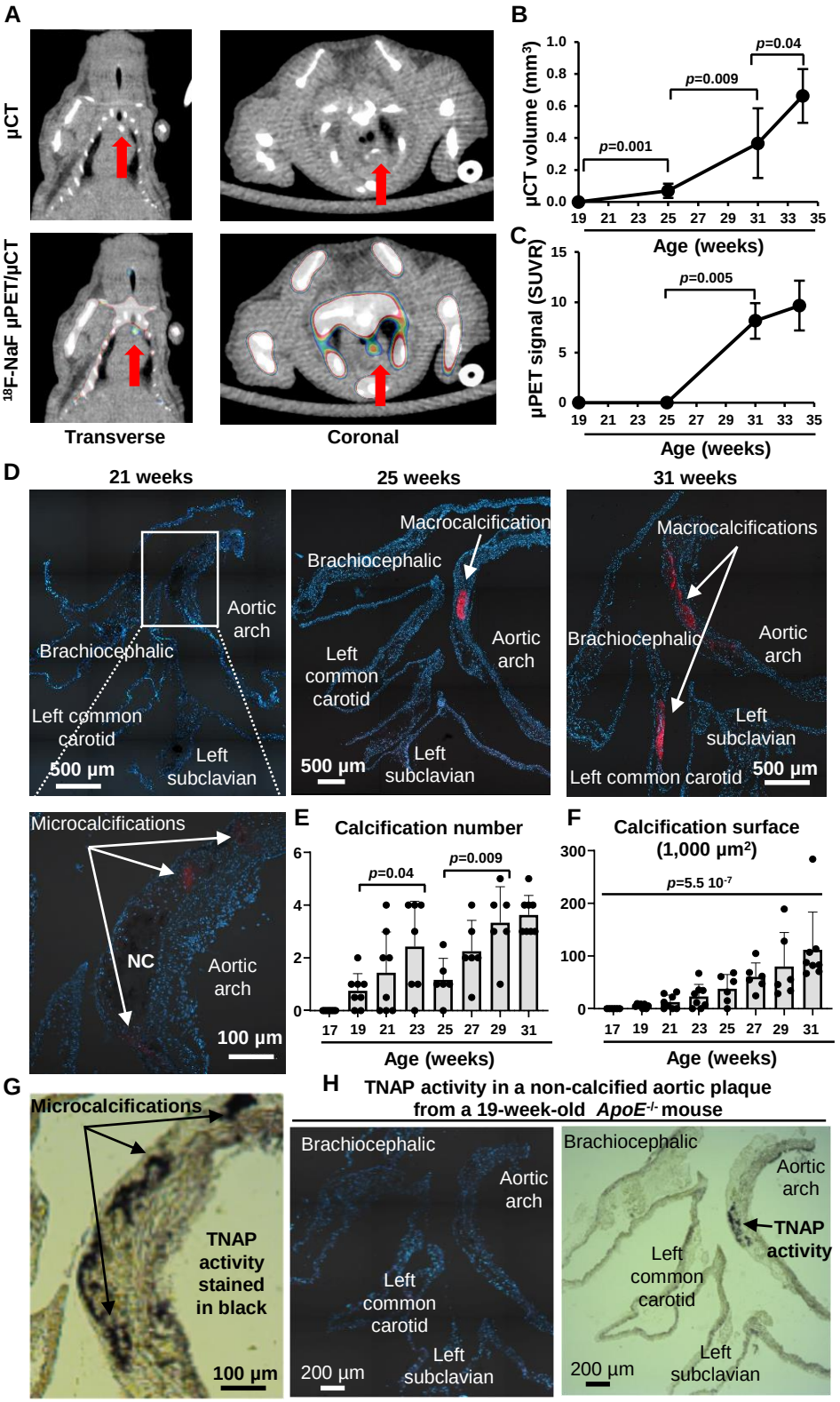


Figure 2

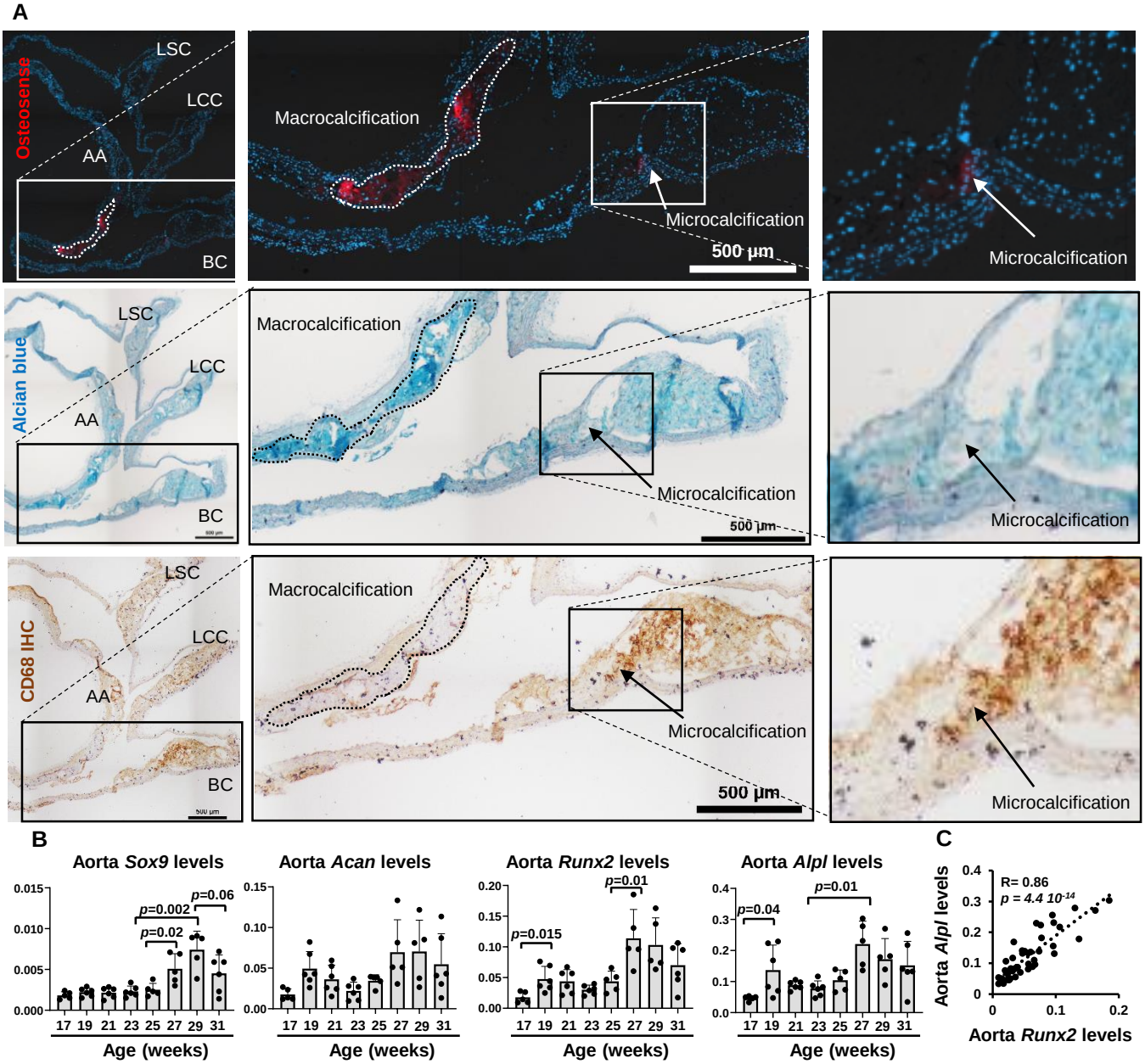

A
Osteosense
LSC
LCC
AA
BC
Macrocalcification
Microcalcification
500 µm
Alcian blue
CD68 IHC
B
Aorta Sox9 levels
Aorta Acan levels
Aorta Runx2 levels
Aorta Alpl levels
p=0.06
p=0.002
p=0.02
p=0.015
p=0.01
p=0.04
Age (weeks)
C
Aorta Alpl levels
Aorta Runx2 levels
R= 0.86
p = 4.4 10-14

Figure 3

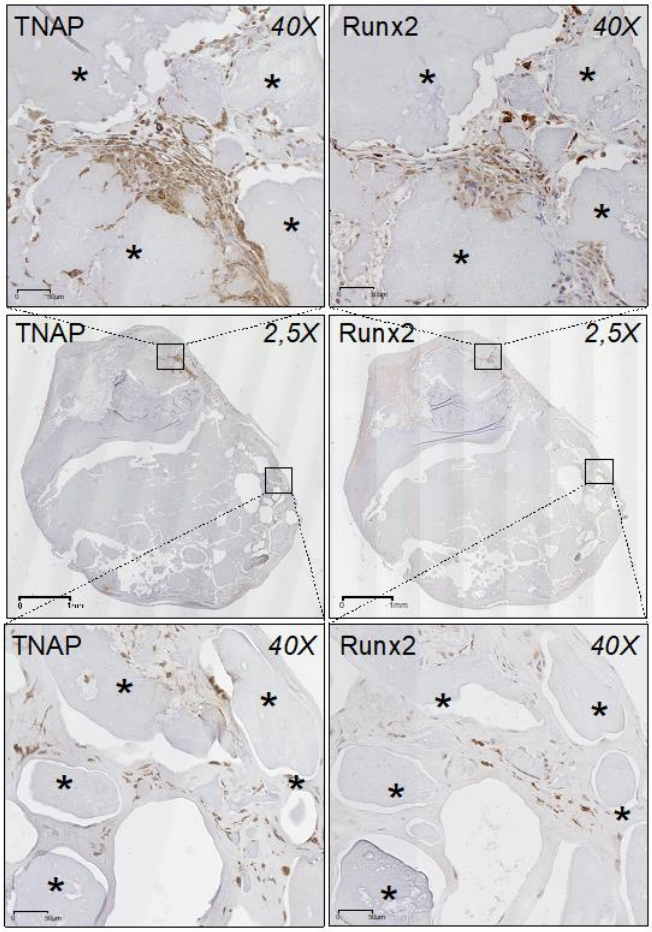


Figure 4

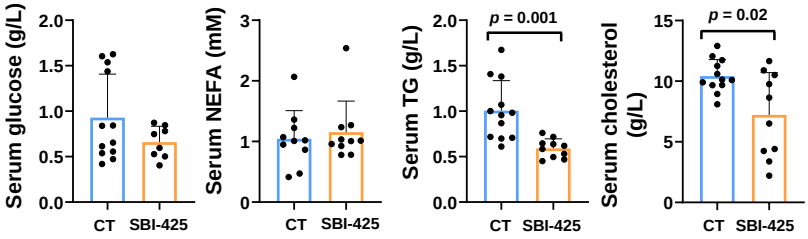
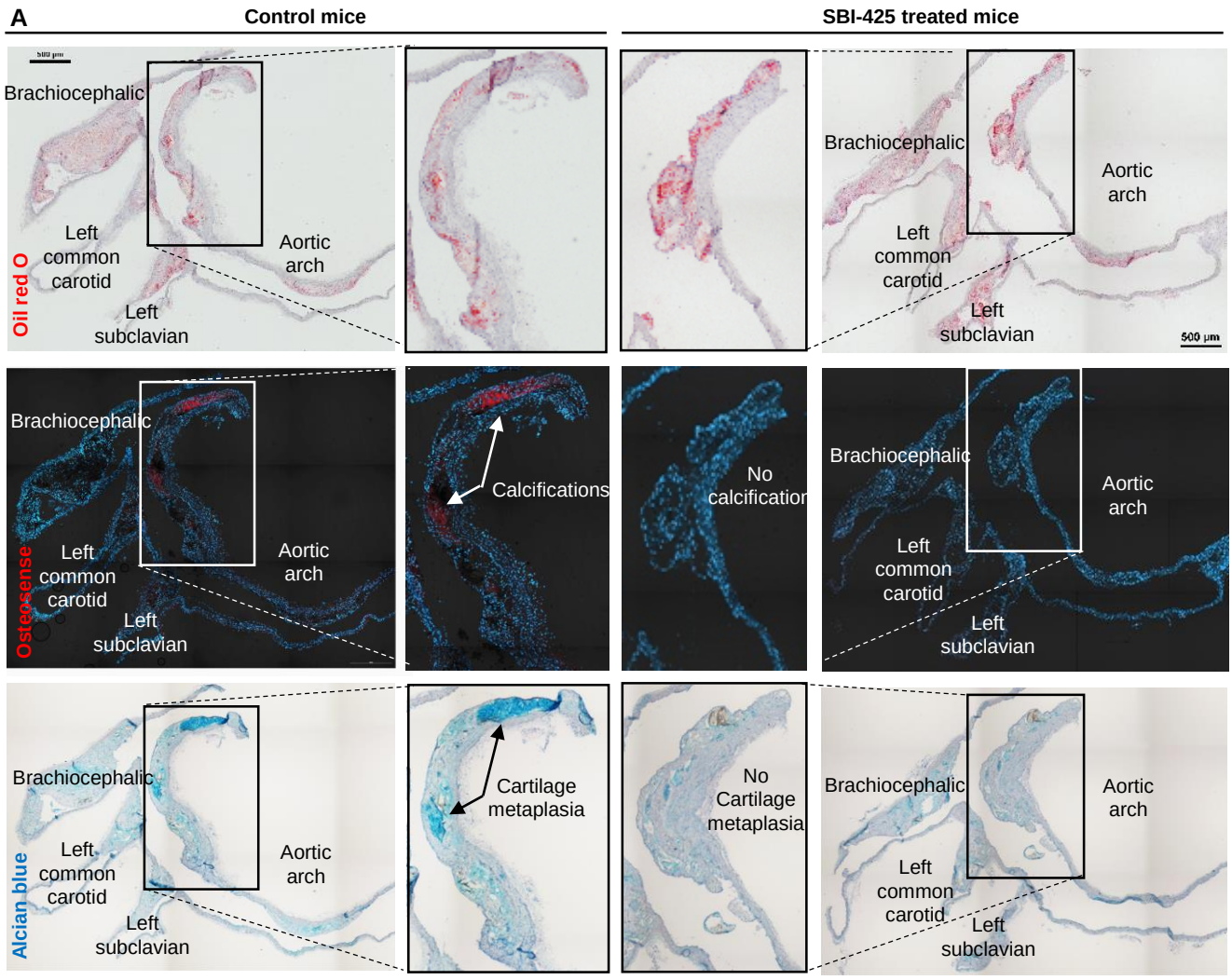

Serum glucose (g/L)
2.0
1.5
1.0
0.5
0.0
CT
SBI-425
Serum NEFA (mM)
3
2
1
0
CT
SBI-425
Serum TG (g/L)
p = 0.001
2.0
1.5
1.0
0.5
0.0
CT
SBI-425
Serum cholesterol (g/L)
p = 0.02
15
10
5
0
CT
SBI-425

Figure 5


A
Control mice
SBI-425 treated mice
Brachiocephalic
Left common carotid
Aortic arch
Left subclavian
Oil red O
Osteosense
Alcian blue
Calcifications
No calcification
Cartilage metaplasia
No Cartilage metaplasia
500 µm

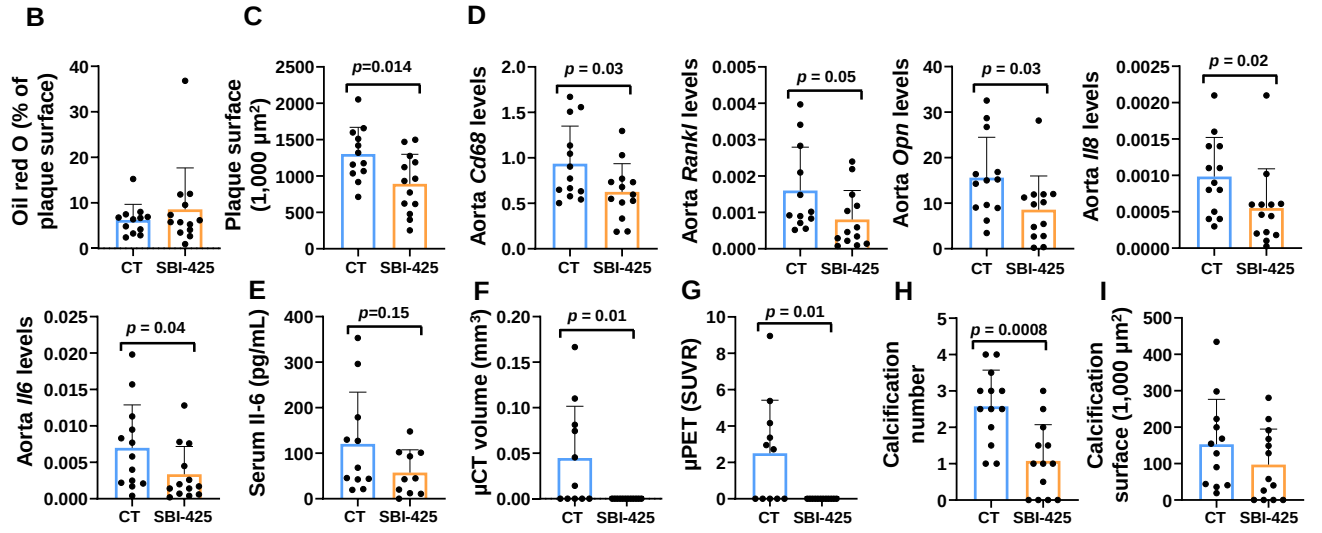
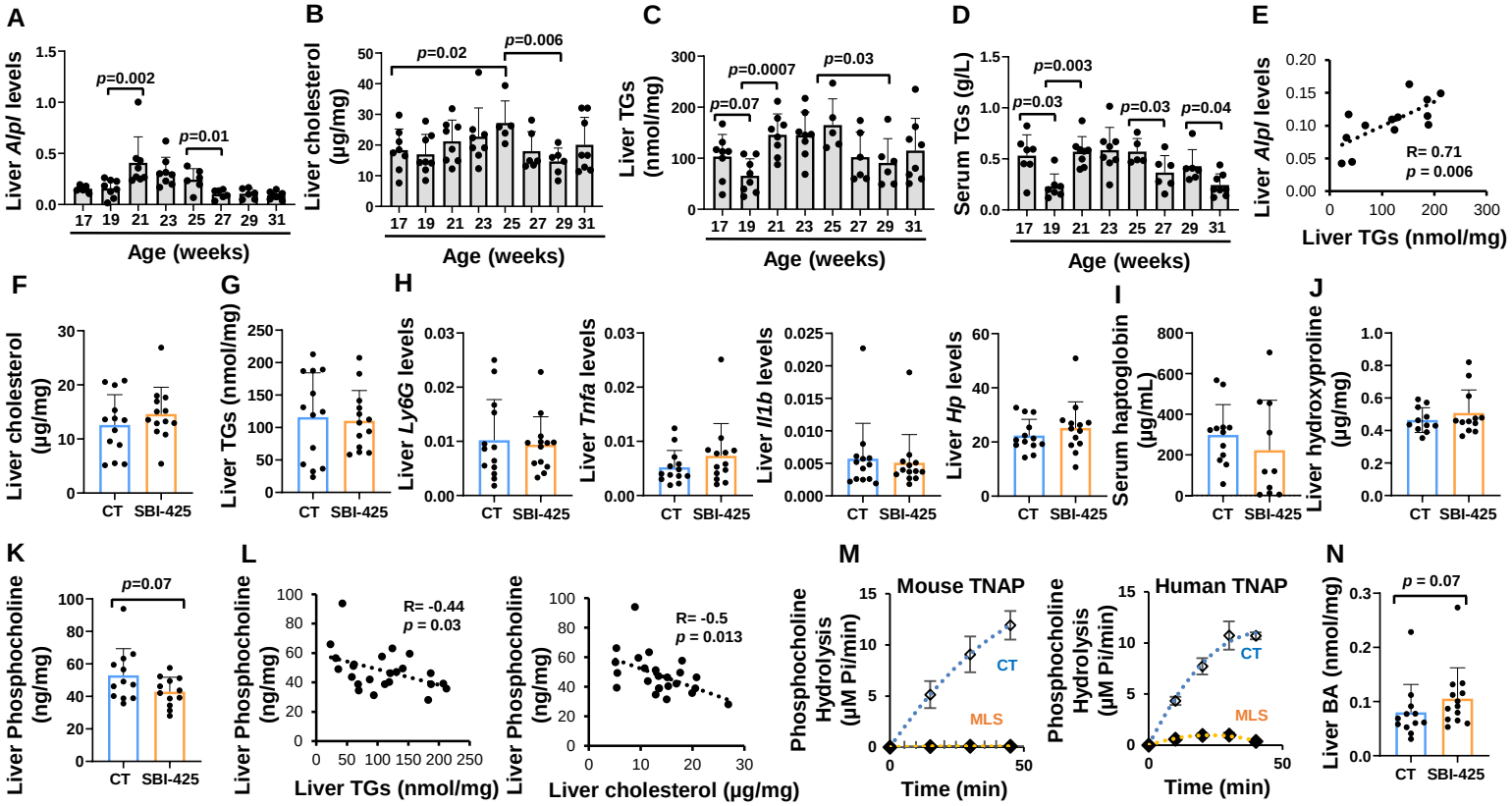
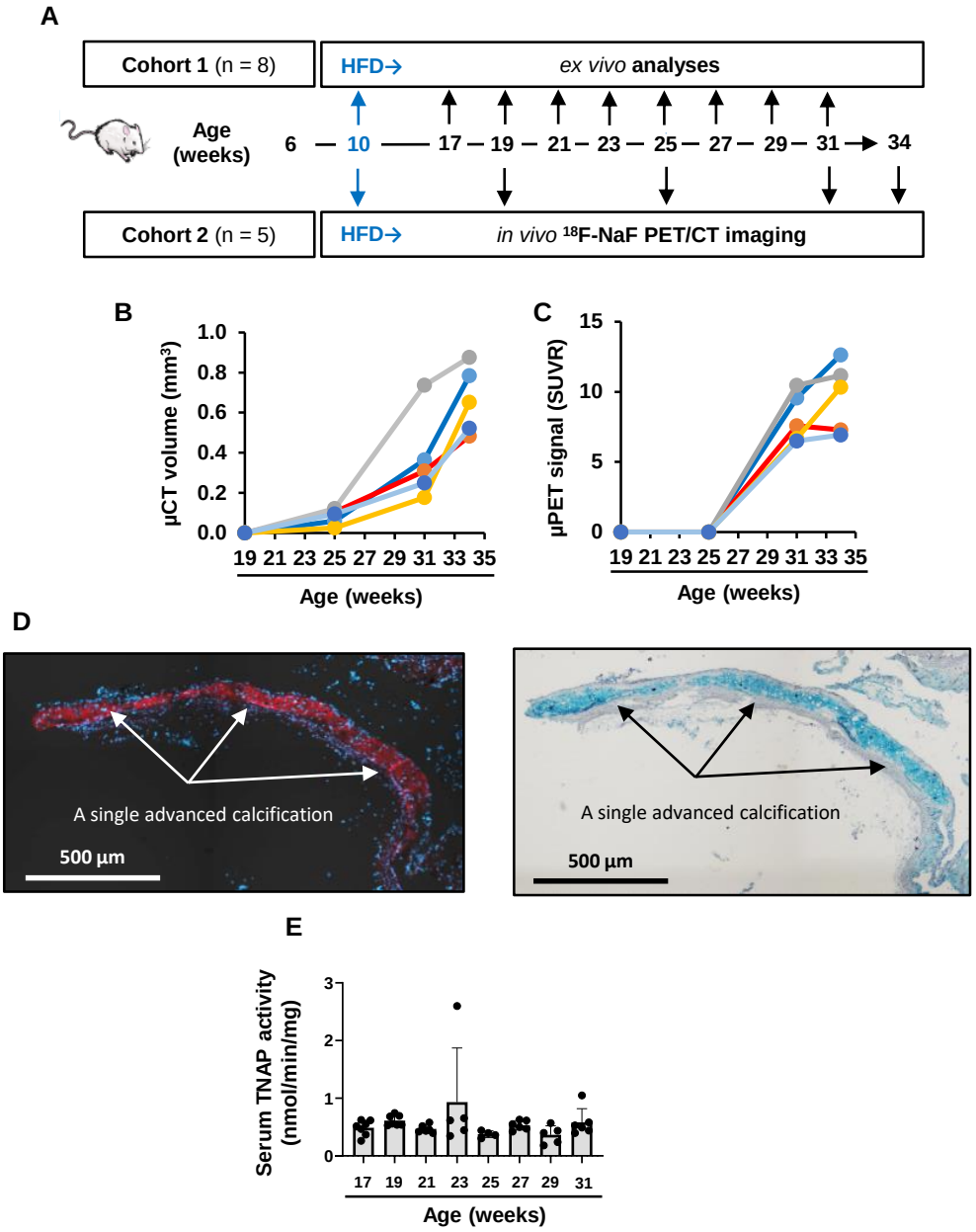

B
Oil red O (% of plaque surface)
C
Plaque surface (1,000 µm²)
p=0.014
D
Aorta Cd68 levels
p = 0.03
Aorta Rankl levels
p = 0.05
Aorta Opn levels
p = 0.03
Aorta Il8 levels
p = 0.02
Aorta Il6 levels
p = 0.04
E
Serum Il-6 (pg/mL)
p=0.15
F
µCT volume (mm³)
p = 0.01
G
µPET (SUVR)
p = 0.01
H
Calcification number
p = 0.0008
I
Calcification surface (1,000 µm²)
CT
SBI-425

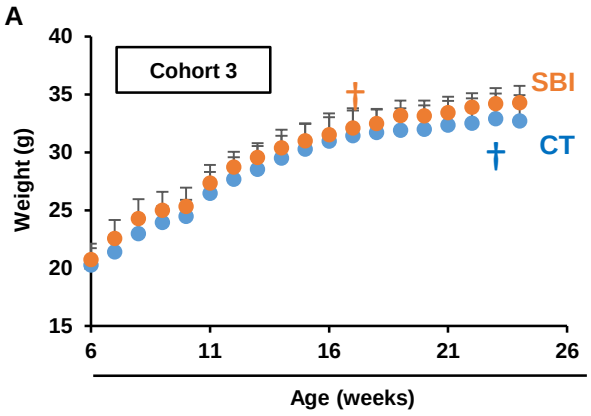
Figure 6

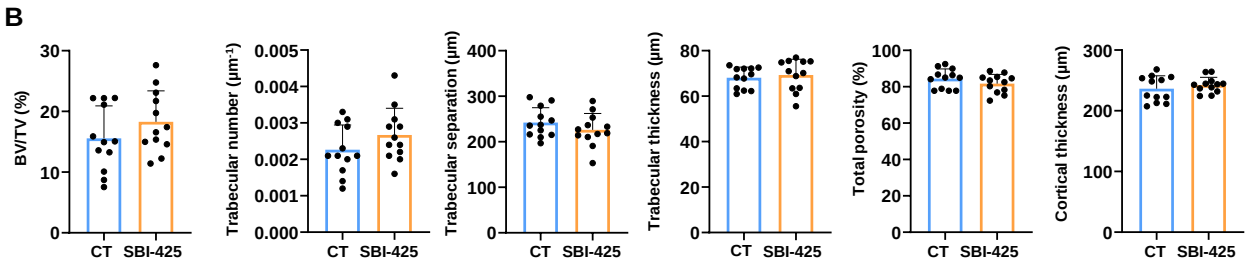

A
Liver Alpl levels
p=0.002
p=0.01
Age (weeks)
B
Liver cholesterol (µg/mg)
p=0.02
p=0.006
Age (weeks)
C
Liver TGs (nmol/mg)
p=0.07
p=0.0007
p=0.03
Age (weeks)
D
Serum TGs (g/L)
p=0.03
p=0.003
p=0.03
p=0.04
Age (weeks)
E
Liver Alpl levels
R= 0.71
p = 0.006
Liver TGs (nmol/mg)
F
Liver cholesterol (µg/mg)
G
Liver TGs (nmol/mg)
H
Liver Ly6G levels
Liver Tnfa levels
Liver Il1b levels
I
Liver Hp levels
Serum haptoglobin (µg/mL)
J
Liver hydroxyproline (µg/mg)
CT
SBI-425
K
Liver Phosphocholine (ng/mg)
p=0.07
L
Liver Phosphocholine (ng/mg)
R= -0.44
p = 0.03
Liver TGs (nmol/mg)
R= -0.5
p = 0.013
Liver cholesterol (µg/mg)
M
Mouse TNAP
Human TNAP
Phosphocholine Hydrolysis (µM Pi/min)
CT
MLS
Time (min)
N
Liver BA (nmol/mg)
p = 0.07

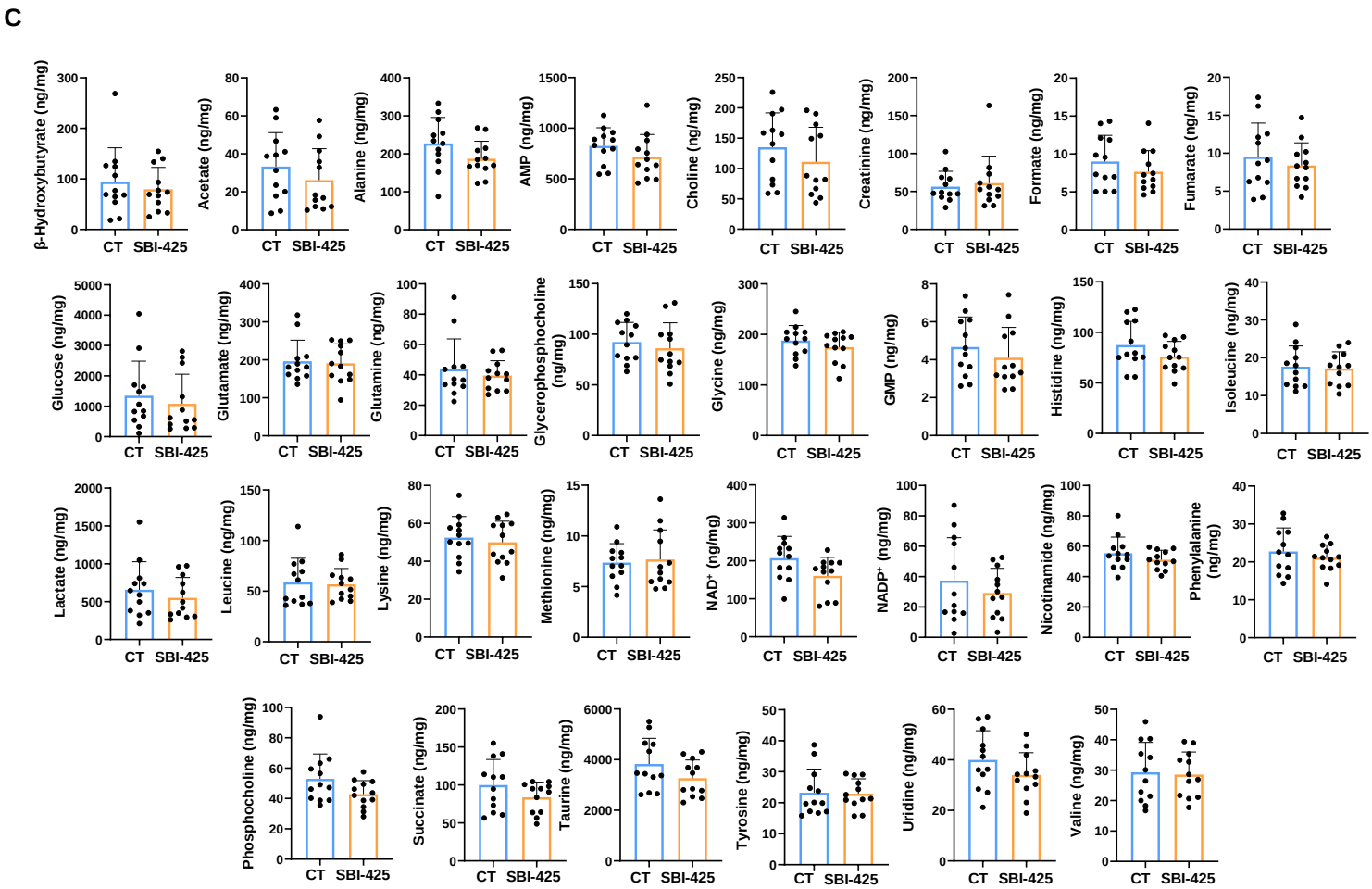
Supplemental Figure 1



Supplemental Figure 2







Supplemental Figure 3

